



HAL
open science

Effect of an Aromatic Sulfonate Ligand on the Photovoltaic Performance of Molybdenum Cluster-Sensitized Solar Cells

Thi Kim Ngan Nguyen, Satoshi Ishii, Adèle Renaud, Fabien Grasset, Stéphane Cordier, Noe Dumait, Hiroshi Fudouzi, Tetsuo Uchikoshi

► **To cite this version:**

Thi Kim Ngan Nguyen, Satoshi Ishii, Adèle Renaud, Fabien Grasset, Stéphane Cordier, et al.. Effect of an Aromatic Sulfonate Ligand on the Photovoltaic Performance of Molybdenum Cluster-Sensitized Solar Cells. ACS Applied Energy Materials, 2024, Acs Applied Energy Materials, 7 (2), pp.760-773. 10.1021/acsaem.3c02823 . hal-04395221

HAL Id: hal-04395221

<https://hal.science/hal-04395221>

Submitted on 16 Jan 2024

HAL is a multi-disciplinary open access archive for the deposit and dissemination of scientific research documents, whether they are published or not. The documents may come from teaching and research institutions in France or abroad, or from public or private research centers.

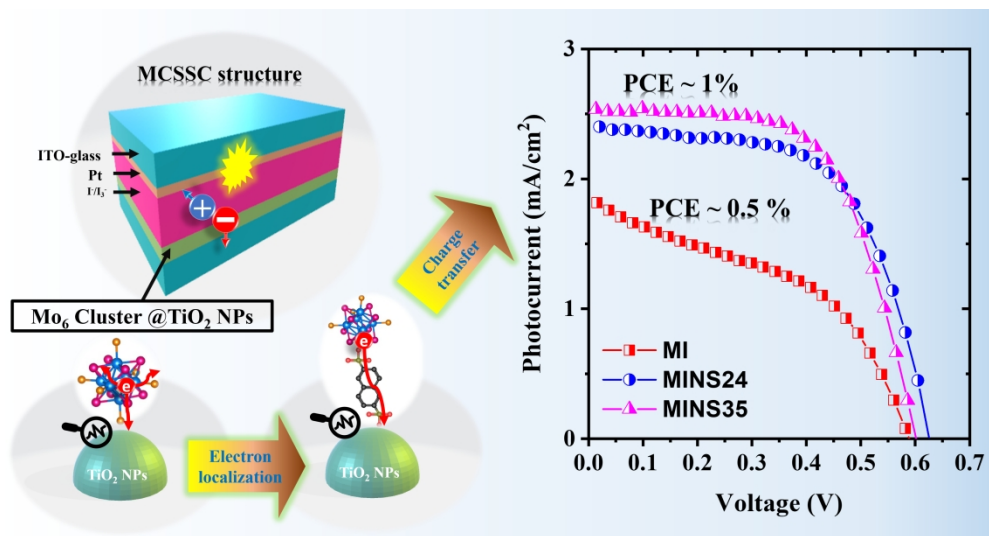
L'archive ouverte pluridisciplinaire **HAL**, est destinée au dépôt et à la diffusion de documents scientifiques de niveau recherche, publiés ou non, émanant des établissements d'enseignement et de recherche français ou étrangers, des laboratoires publics ou privés.

This document is confidential and is proprietary to the American Chemical Society and its authors. Do not copy or disclose without written permission. If you have received this item in error, notify the sender and delete all copies.

Effect of Aromatic Sulfonate Ligand on the Photovoltaic Performance of Molybdenum Cluster-Sensitized Solar Cell

Journal:	<i>ACS Applied Energy Materials</i>
Manuscript ID	ae-2023-02823y.R1
Manuscript Type:	Article
Date Submitted by the Author:	11-Dec-2023
Complete List of Authors:	NGUYEN, Thi Kim Ngan; National Institute for Materials Science, Fine Particle Engineering Ishii, Satoshi; Busshitsu Zairyo Kenkyu Kiko, International Center for Materials Nanoarchitectonics Renaud, Adèle; Institut des Sciences Chimiques de Rennes, Grasset, Fabien; CNRS, UMI3629 Cordier, Stéphane; UMR 6226 CNRS-Universite de Rennes 1, Chemistry Dumait, Noee; UMR 6226 CNRS-Universite de Rennes 1, Chemistry Fudouzi, Hiroshi; National Institute for Materials Science Research Center for Functional Materials, Colloidal crystal materials group UCHIKOSHI, Tetsuo; National Institute for Materials Science, Research Center for Functional Materials

SCHOLARONE™
Manuscripts



The schematic illustration of MCSSC and chemical structure of the Mo₆ cluster on TiO₂ and J-V characteristics of the MCSSCs composed of the Mo₆ cluster-based-sensitizers

656x349mm (150 x 150 DPI)

Effect of Aromatic Sulfonate Ligand on the Photovoltaic Performance of Molybdenum Cluster-Sensitized Solar Cell

Thi Kim Ngan Nguyen^{1,*}, Satoshi Ishii², Adèle Renaud³, Fabien Grasset^{3,4}, Stéphane Cordier³, Noée Dumait³, Hiroshi Fudouzi⁵, Tetsuo Uchikoshi^{4,5}

¹International Center for Young Scientists, Global Networking Division, National Institute for Materials Science, 1-2-1 Sengen, Tsukuba, Ibaraki 305-0044, Japan

²Research Center for Materials Nanoarchitectonics (MANA), National Institute for Materials Science, 1-1 Namiki, Tsukuba, Ibaraki 305-0044, Japan

³Univ. Rennes-CNRS-Institut des Sciences Chimiques de Rennes, UMR6226, 35000 Rennes, France

⁴CNRS–Saint-Gobain–NIMS, IRL3629, Laboratory for Innovative Key Materials and Structures, National Institute for Materials Science, 1-1 Namiki, Tsukuba, Ibaraki 305-0044, Japan

⁵Research Center for Electronic and Optical Materials, National Institute for Materials Science, 1-2-1 Sengen, Tsukuba, Ibaraki 305-0044, Japan

Corresponding author: Thi Kim Ngan NGUYEN

Full postal address: International Center for Young Scientists, National Institute for Materials Science (NIMS), 1-2-1 Sengen, Tsukuba, Ibaraki 305-0047, Japan

E-Mail address: NGUYEN.Thikimngan@nims.go.jp

Abstract

The photovoltaic performance of molybdenum cluster-sensitized solar cells (MCSSCs) has been explored with the challenge of enhancing their efficiency due to the low charge transfer efficiency. Aromatic sulfonate ligands (NS = naphthalene 2,6-disulfonate = $^{-}\text{OSO}_2\text{-C}_{10}\text{H}_6\text{-SO}_3^{-}$) were now used for the functionalization of the $\{\text{Mo}_6\text{I}_8\}$ cluster cores. The new functional $[\text{Mo}_6\text{I}_8\text{I}_3(\text{H}_2\text{O})_2(\text{NS}^-\text{Na}^+)]^a$ cluster unit exhibits enhanced photophysical and photoelectrochemical properties compared to other homologues based on the $\{\text{Mo}_6\text{I}_8\}$ cluster cores. In greater detail, the role of the NS functional groups was beneficially emphasized for the improved oxidation stability of the cluster in a redox mediator, adjusting of the emission lifetime to a suitable range for fast electron injection, and accelerating the charge transport process. The best as-synthesized Mo_6 cluster-based solar cell resulted in a stable photocurrent of $2.38 \text{ mA}\cdot\text{cm}^{-2}$ with a fill factor of 0.63 and the power conversion efficiency of 0.97%

1
2
3
4
5
6 under AM 1.5 illumination, a 2 times enhancement in comparison to the reference iodide Mo₆ cluster-
7 based cell (0.52 %). Specific attention focused on the increase of the power conversion efficiency up
8 to 1.18 % after 330 seconds, then reached the saturation trend. The enhanced charge transfer of the
9 metal cluster complex was obtained from facile modifications of the functional apical ligands that
10 result in advantageous photophysical and electrochemical characteristics specializing in
11 optoelectronic devices. This study provides the general methodology and knowledge for the next
12 improvement of the photovoltaic efficiency of the Mo₆ cluster-based sensitized solar cells.
13
14
15
16
17
18

19 Keywords: molybdenum cluster, optoelectronic, charge transfer, solar cell, photoluminescent lifetime.
20
21
22

23 1. Introduction

24 With attention to reducing fossil fuels in energy production, scientists are now evaluating new
25 materials and technologies for converting solar light energy into electricity [1]. The high cost of
26 manufacturing and raw materials of Si-based solar technology leads to the exploration of third-
27 generation photovoltaic devices with emerging solar cells based on low-cost and abundant materials,
28 ease of shaping, and flexible design. This photovoltaic generation involves various technologies, such
29 as organic, perovskite, or organic–inorganic hybrid perovskite solar cells, differing by the nature of
30 the photoelectrode materials [2-4]. Dye-sensitized solar cells (DSSCs), quantum dot-sensitized solar
31 cells (QDSSCs), and metal cluster-sensitized solar cells (MCSSCs) are based on the same design. They
32 contained two electrodes, a photoanode based on the transparent semiconductor layers recovered by
33 molecular light-harvesters, i.e. organic dyes, quantum dots, or metal clusters, and a metallic counter
34 electrode, separated by an electrolyte composed of a redox mediator. The emergence of light-harvester-
35 sensitized solar cells was developed by Grätzel and his colleagues in 1991, resulting in an impressive
36 power converting efficiency (PCE) of 7.9 % [5]. Since then, many studies based on the development
37 of 0-3D nanostructured semiconductors, photosensitizers, counter electrodes, redox electrolytes, and
38 device architectures have allowed improving the energy conversion efficiency of the DSSCs [6-8].
39 The best photovoltaic performance (η %) of DSSCs recently reported 15.2 % under 1.5 global
40 simulated sunlight, while it is 15.31 % recorded for QDSSCs [9-10].
41
42
43
44
45
46
47
48
49
50
51
52
53

54 In the dynamics of exploring new potential sensitizers, metal atom clusters were introduced as light-
55 harvesting materials in the MCSSCs. The Au, Pt, Pd, and Ag-based metal clusters have been
56 investigated which led to the overall efficiencies of 2.4 % for thiolate gold, 1.1 % for silver-copper
57
58
59
60

1
2
3
4
5
6 nanoalloy, and 0.26 % for Ag₁₆(SG)₉ nanoclusters [11-13]. However, the limitation of MCSSCs based
7 on these metal clusters was a lower absorption in the visible range. The photosensitizer plays an
8 important role since it absorbs the light energy for supplying photo-excited electrons to generate the
9 photocurrent. Therefore, many efforts have been made to strengthen the function of the sensitizers
10 such as i) absorption in the visible light range, ii) the quenching of the photoexcited electron, iii) the
11 stabilization and regeneration of sensitizer in the redox mediator, and iv) the beneficial electron
12 transfer and electron lifetime in the redox electrolyte [14-17].

13
14
15
16
17
18 A metal cluster family with a unique electron structure has been introduced as a broadly visible light
19 absorber. The face-capped [(Mo₆X₈)L₆]⁻² cluster (Xⁱ = halogen, L^a = halogen, functional groups, H₂O,
20 etc.) was built on an octahedral Mo₆ cluster that bonded with 8 inner ligands in face-capping positions
21 and 6 apical ligands in terminal positions [18-20]. The charge of the negatively charged cluster was
22 balanced by inorganic or organic counter-cations (e.g.; alkali cation or quaternary ammonium) [21-
23 22]. The nanosized Mo₆ cluster appeared attractive as a photosensitizer due to its high photostability,
24 large Stoke shift for reducing the absorbing energy, and feasible modification of the chemical
25 composition for adjusting the optical bandgap [18, 23]. The Mo₆ cluster was able to create a
26 photoexcited electron under visible light irradiation, however, the material itself limited charge
27 transfer for optoelectronic applications. For this reason, the incorporation of the Mo₆ cluster with a
28 semiconductor has essentially been studied to enhance the charge transfer via covalent bonds or ionic
29 interactions. Several designs have been studied using TiO₂ for solar cells, double layer hydroxides or
30 tin pyrophosphate semiconductors for photoconductivity sensors, and graphene oxide for enhanced
31 photoinactivation [18, 24-26].

32
33
34
35
36
37
38
39
40
41
42 Recently, a general study revealed the photovoltaic efficiency of the Mo₆ cluster as an absorber in n
43 and p-type solar cells prepared by using an electrophoretic deposition process (EPD), resulting in the
44 best performance efficiency of 0.44 % [18-19, 27]. The lack of knowledge about the photophysical
45 and photoelectrochemical behaviors of the Mo₆ cluster in the redox mediator of MCSSCs inspired the
46 investigation of the study. According to the Shockley-Queisser (SQ) limitation for a single p-n junction,
47 the optimal band gap (E_g) of the absorber is situated around 1.3 eV [28]. In a previous study, the band
48 gap of the Mo₆ cluster iodides was measured at 1.9 eV and it is stable when iodide apical ligands of
49 the Cs₂[(Mo₆I₈)I₆] precursor were replaced by several water molecules to form the [Mo₆I₈I₄
50 (H₂O)₂].x H₂O cluster [19, 24, 27]. By integrating such Mo₆ clusters as sensitizers in n- and p-type
51 MSSCs, a proof of concept was obtained. Such molecular clusters can be used as light harvesters to
52
53
54
55
56
57
58
59
60

1
2
3
4
5
6 photoinduce both electron and hole transfers. The ambipolar behavior of such Mo₆-based layers was
7 more recently demonstrated [27]. However, with a short-circuit (J_{sc}) current of 1.13 mA.cm⁻² and an
8 open circuit (V_{oc}) of 529 mV, the recorded performances were low [19]. They were attributed to a non-
9 effective charge transfer. The iodide Mo₆ cluster had a weak photoluminescence, however, its emission
10 lifetime was beneficially revealed in the microsecond range [20]. The photophysical properties,
11 absorbance, and photoluminescence could be modified by the nature of the inner and/or apical ligands
12 and affected by the number of valent electrons in a cluster unit [20]. This study confirmed a relative
13 relation between the chemical composition of the apical ligands of the cluster and the emission lifetime.
14 A photosensitizer should be luminescent with a favorably long emission lifetime in a range between
15 μ s and ns, being faster than the process of charge injection (0.1 ns) [2]. With the emission lifetime in
16 the microsecond range, the photoexcited electrons on the Mo₆ cluster are able to be injected into the
17 conduction band of the semiconductor electrode in the MCSSCs. Although the Mo₆ clusters do not
18 have an optimal absorption in the visible range when compared to porphyrin; for example, a broad
19 absorbing spectrum, limited self-quenching of the excited state at a high concentration and low
20 photobleaching it can compensate for these drawbacks [29].
21
22
23
24
25
26
27
28
29
30
31
32

33 Under these circumstances, the goal of this study is to introduce functional groups at the terminal
34 positions of the Mo₆ cluster for i) improving the interactions of the Mo₆-based sensitizer with the
35 semiconductor substrate, ii) improving the efficiency of electron injection by adjusting the emission
36 lifetime of the photoexcited electrons in the suitable range, and iii) limiting the aggregation of adsorbed
37 clusters which can quench the photoexcited electron. Starting from the Mo₆ cluster iodide precursor
38 Cs₂[{Mo₆I₈}I₆^a], a few iodide ligands were replaced by naphthalene 2,6-disulfonate (NS) organic
39 molecules, composed of electron-donating naphthalene and electron-withdrawing sulfonate for
40 delocalizing the photoinduced electron. An X-ray photoelectron analysis confirmed the chemical
41 compositions of the as-synthesized compounds including the [Mo₆I₈I₃(H₂O)^a₂(-OSO₂-C₁₀H₆-SO₃⁻
42 Na⁺)^a] clusters and free Na₂(-OSO₂-C₁₀H₆-SO₃⁻) molecules with different constitutions that depended
43 on the molar ratios of the Cs₂[{Mo₆I₈}I₆^a] precursor and NS. The replacement of iodide ligands by
44 NS molecules resulted in modification of the band gaps with the shift from 2.08 eV to 2.60 eV and
45 increased the radiative recombination rate that was indicated by a broad peak centered around 640 nm
46 in the photoluminescence spectra. The radiative recombination time of the modified Mo₆ cluster was
47 adjusted in the suitable range (ns < τ < μ s) for photovoltaic cells, the longer than electron injection
48
49
50
51
52
53
54
55
56
57
58
59
60

1
2
3
4
5
6 time (~ 0.1 ns), and shorter than the cluster regeneration time (~ 0.1 μ s) in the electrolyte mediator [2].
7
8 The photovoltaic properties were systematically studied to reveal the role of NS at different
9
10 compositions on isolated and non-isolated Mo₆ cluster-based nanocomposites. Both the
11
12 [Mo₆I₈I₃(H₂O)^a₂(-OSO₂-C₁₀H₆-SO₃⁻ Na⁺)^a] clusters and free Na₂(-OSO₂-C₁₀H₆-SO₃⁻) molecules
13
14 contributed to the enhancement of the homogeneous dispersion of the Mo₆ cluster and charge
15
16 transferring rate such that the power conversion efficiency (PCE = 0.97 %) increased by a factor of 2
17
18 compared to a previous study (0.44 %) [19]. This is a new record of efficiency for Mo₆-based cluster-
19
20 sensitized solar cells. The Mo₆ cluster-based cells resulted in an impressive accumulation of the
21
22 photocurrent while the NS at a good concentration can retain the enhanced photocurrent in the MINS-
23
24 based cells. With regard to this, an increase in PCE by about 20 % after the first 5 minutes of the AM
25
26 1.5G illumination was recorded until it reached saturation. These promising results open the door for
27
28 the investigation of the octahedral transition metal clusters as a new nontoxic light harvester for
29
30 photoelectrochemical devices ranging from sensitizer solar cells to solid solar cells.

31 2. Experimental sections

32 Chemicals

33 Acetone (99.5 %) and acetonitrile were supplied from Nacalai Tesque. The titanium chloride solution
34
35 (TiCl₄, 16.0~17.0 % as Ti) and disodium naphthalene-2,6-disulfonate were purchased from the
36
37 Fujifilm Wako Pure Chemical Collaboration. Ti-Nanoxide T/SP, which contains anatase titanium
38
39 dioxide particles with a size of about 15-20 nm and a concentration of 18 wt%, was purchased from
40
41 Solaronix. The compositions of the electrolytes that included I₂, LiI, 1-butyl-3-methylimidazolium
42
43 iodide, and (2) 4-tertbutylpyridine were purchased from Sigma-Aldrich. All the chemicals were used
44
45 without purification. The deionized water was obtained using Water Purifiers WG710 equipment with
46
47 conductance of 0.5×10^{-4} S/m at 25°C. The Cs₂[{Mo₆I₈}I₆^a] (CMI) cluster powder was synthesized by
48
49 the solid-state procedure reported in a previous publication without purification [30].

50 Modification of apical ligand of Cs₂[{Mo₆I₈}I₆^a] (CMI) cluster

51
52 The Cs₂[{Mo₆I₈}I₆^a] (CMI) cluster precursor was dissolved in acetone (1 g/L) and the naphthalene
53
54 2,6-disulfonate (NS) organic molecule was separately dissolved in distilled water at room temperature
55
56 under ambient conditions. The molar ratios are listed in Table SII. Both solutions were then mixed at
57
58 70°C for 3 hours and continually stirred at room temperature for 48 hours. The transparent and red-
59
60

1
2
3
4
5
6 colored solution containing CMI shifted to a slightly turbid orange. The slurries were abbreviated as
7 non-isolated MINS_x with $x=16, 24, \text{ and } 35$, and x as an abbreviated representation of the molar ratios
8 between NS and the CMI precursors. (**Tab. S1**). In addition, all the MINS_x slurries were purified by
9 washing four times in an acetone/water mixture to remove any residual substances, then heated at 50°C
10 for 24 hours, and abbreviated as isolated MINS_x with $x=16, 24, \text{ and } 35$. All the prepared composites
11 were stored at 50°C for the next steps and deposited on quartz glass for characterization.
12
13
14
15
16
17

18 Preparation of the Mo₆ cluster-based photoelectrodes

19 The mesoporous titanium dioxide (TiO₂) film was prepared on a highly durable transparent conductive
20 ITO glass (Geomatec Co., Ltd., Tokyo, Japan; < 5 Ohm/sq). the 2×3 cm² ITO glass was first properly
21 washed using acetone and ethanol, then coated with a commercial Ti-Nanoxide paste by the doctor
22 blade technique with a thickness of about 5μm. Afterward, the TiO₂ paste-based photoelectrode was
23 sintered at 450 °C for 1 hour in ambient air to decompose the unnecessary organic compositions, then
24 cooled to room temperature. A titanium (IV) chloride surface (TiCl₄) treatment was performed on the
25 mesoporous TiO₂ film that was referenced from a previous procedure to enhance the charge transport
26 [31]. The electrodes were immersed in a TiCl₄ solution (0.3 M) of distilled water at 70 °C for 30 min.
27 The electrode was then washed using distilled water to remove the white TiO₂ nanoparticles on the
28 surface, then sintered at 450 °C for 30 min in ambient air. The active TiO₂ area for the absorbing
29 photosensitizer was 1.2×1.5 cm². The non-isolated MINS_x ($x=16, 24, 35$) suspensions were directly
30 poured into a 500 mL beaker and stabilized in a vacuum impregnation apparatus. The TiCl₄-treated
31 TiO₂ mesoporous film was immersed in the photosensitizer-containing beaker for 15 minutes under
32 vacuum pressure (~ 6 Pa). The photoelectrode was then heated at 120 °C for 30 minutes to properly
33 eliminate the solvent and perform possible covalent bonding between the TiO₂ and Mo₆ cluster-based
34 photosensitizer. A negative MI nanocluster was also deposited on the TiO₂ electrode by electrophoretic
35 deposition (EPD) at 20 V for 2 minutes as in the illustration below. The EPD system consisted of one
36 indium tin oxide-coated glass slide with a surface area of 2×3 cm² acting as the cathode and one TiCl₄-
37 treated TiO₂ mesoporous film acting as an anode that was connected to a Source Meter (Keithley
38 Model 2400, Ohio, USA) as an electric field generator. All the TiO₂ photoelectrodes adsorbed Mo₆
39 cluster-based photosensitizers were stored at 50 °C before characterization.
40
41
42
43
44
45
46
47
48
49
50
51
52
53
54
55
56
57

58 Solar cell fabrication

1
2
3
4
5
6 The n-MCSCs were an assembled structure of two photoelectrodes with filtered electrolytes in the
7 middle space. A counter electrode was prepared by quickly coating a platinum layer at a current of 5
8 mA for 5 minutes under plasma treatment. The TiCl₄-treated TiO₂ photoanode coated with
9 photosensitizers was sealed with a platinum-coated ITO glass using a Surlyn polymer spacer (Meltonix
10 1170-25, 25 μm) at 120 °C for 10 minutes. The electrolyte composed of the iodide/triiodide couple
11 was referenced from the previous report with a slight modification for comparison [19]. The redox
12 mediator compositions included 0.05 M I₂, 0.1 M LiI, 0.6 M 1-butyl-3-methylimidazolium iodide, and
13 0.5 M (2)4-tertbutylpyridine in acetonitrile. The J-V characteristic was recorded by a Keithley 2400
14 source meter under the illumination of one sun (AM 1.5G illumination, HAL-320, Asahi Spectra USA,
15 Inc.) with a power density of 100 mW.cm⁻².

16
17
18
19
20
21
22
23 The overall efficiency (PCE, %) is the percentage of the solar energy converted into electrical energy
24 under the illumination of one sun calculated using equation (1) [2]:

$$\eta (\%) = \frac{J_{sc} \times V_{oc} \times FF}{P_{in}} \quad (1)$$

25
26
27
28
29
30
31
32
33
34 where J_{sc} is the current per active area recorded using a source meter (2400, Keithley) under the
35 illumination of one sun (AM 1.5G illumination) with a P_{in} of 100 mW.cm⁻². V_{oc} and FF are the open
36 circuit voltage and fill factor, respectively.

37
38
39
40
41
42
43
44
45
46
47
48
49
50
51
52
53
54
55
56
57
58
59
60
The incident photon-to-current conversion efficiency (IPCE) of the n-MCSC was calculated using
equation (2) [2]:

$$IPCE = \frac{J_{sc} \times 1240}{P_{in} \times \lambda} \quad (2)$$

where J_{sc} is the photocurrent per active area recorded using a source meter (2400, Keithley) under the
illumination of a wavelength-tunable light source (NIJI-2, Bunkoukeiki) with P_{in} (mW/cm²), and λ is
the corresponding excitation wavelength.

Material characterizations

The binding energy spectra were measured by X-ray photoelectron spectroscopy (XPS) (PHI Quantera
SXM (ULVAC-PHI)) using Al Kα radiation at 20 kV and 5 mA and the binding energies were
calibrated with the C1s peak at 285 eV. The typical chemical vibrations were verified by Raman
spectroscopy (RAMAN plus, Nanophoton Co., Ltd., Japan) in the wavenumber range from 0 to 1800
cm⁻¹ under the excitation of the laser wavelength of 532 nm and Fourier transform infrared
spectroscopy (FTIR) (Thermo Scientific Nicolet 4700) in the wavenumber range from 4000 to 400

1
2
3
4
5
6 cm^{-1} . The crystallinity of the mesoscopic TiO_2 photoelectrode was determined by powder X-ray
7 diffraction (XRD) (SmartLab, RIGAKU, 40 kV and 30 mA) in the 2θ angle range from 20° to 60° for
8 the thin film at the scan speed of $1^\circ/\text{min}$ with the $\text{Cu K}\alpha$ radiation ($\lambda = 1.54 \text{ \AA}$). The absorbance
9 properties were measured by UV-Vis-NIR spectroscopy (JASCO V-650, Jasco Corp.) in the
10 wavelength range of 350 to 1000 nm at the scan rate of 1000 nm/min. The absorbance spectra were
11 used to calculate the optical bandgap (E_g) by using the Tauc relation as demonstrated in the Support
12 Information. The emission spectra were obtained by high-performance fluorescence spectroscopy
13 (JASCO FP8500) connected to a Xenon lamp at the scan rate of 500 nm/min. The surface morphology
14 and the elemental composition were analyzed by field emission scanning electron microscopy (FE-
15 SEM, S4800, Hitachi High-Technologies Corp.) at 10 kV coupled with an energy-dispersive X-ray
16 (EDX) analysis device. The quantum yield was measured by an absolute PL quantum yield
17 spectrometer C11347 (Hamamatsu Corp.) with excitation at a wavelength of 400 nm. Time-resolved
18 photoluminescence (TRPL) signals were recorded via Time-Correlated Single Photon Counting
19 (TCSPC) using HORIBA Scientific fluorescence lifetime systems coupled with a pulsed diode laser
20 (NanoLED-360, Horiba) to excite the samples at the wavelength of 361 nm, pulse duration lower than
21 1 ns, and time-to-amplitude converter (TAC) of 2 ms in an air atmosphere at 298 K.
22
23
24
25
26
27
28
29
30
31
32
33
34

35 Cyclic voltammetry

36 The cyclic voltammetry experiments were carried out in a three-electrode cell including a platinum
37 plate (1 cm^2) as the working electrode, a platinum wire as the counter electrode, and a saturated
38 silver/silver chloride (Ag/AgCl) in 3.5 M KCl as the reference electrode. The Mo_6 cluster prepared by
39 EPD and isolated MINS24 compounds were separately dissolved in acetonitrile at 1 mM, then mixed
40 with the TEABF_4 0.1M supporting electrolyte. The ferrocene/ferrocenium redox system was used as
41 an internal system to calibrate the E^{ox} and E^{red} calculations. The estimated highest occupied molecular
42 orbital (HOMO) and lowest unoccupied molecular orbital (LUMO) energies of the photosensitizers
43 were calculated using the equation: $E_{\text{LUMO}} = -e[(E_{\text{red}} - E_{1/2(\text{ferrocene})} + 4.8) \text{ eV}]$ or $E_{\text{HOMO}} = -e[(E_{\text{ox}} -$
44 $E_{1/2(\text{ferrocene})} + 4.8) \text{ eV}]$ including the ferrocene reference energy level of - 4.8 eV [32]. The half-wave
45 potential $E_{1/2(\text{ferrocene})}$ of the ferrocene/ferrocenium (Fc/Fc^+) redox couple in acetonitrile with the
46 TEABF_4 0.1M supporting electrolyte was found to be 0.448 V (Supporting Information). The solution
47 was degassed by purging with argon for 10 min before measuring. The current gradients were recorded
48 with the potential scanned from -2 V to 2.5 V at 25°C .
49
50
51
52
53
54
55
56
57
58
59
60

Electrical impedance measurement

Impedance measurements were carried out by using a multichannel potentiostat (VSP300, BioLogic Ltd.). The frequency range was from 0.1 Hz to 100 kHz and the alternating signal was 10 mV. The results were recorded with a bias in relation to the V_{OC} of 600 mV in the dark. The obtained spectra were fitted using Z-View software corresponding to the appropriate equivalent circuit.

3. Results and discussions

Effect of NS on the chemical and photophysical properties of isolated composites based on Mo_6 cluster

It was suspected that the halogen groups of the $[Mo_6I_8]^{2-}$ cluster unit hinder the charge transport in photovoltaic devices due to the difficulty in creating covalent bonding with functional groups on the lattice of the semiconducting surface. In order to improve the interactions between the cluster-based sensitizer and the charge collector surface, the replacement of the apical iodide ligands by aromatic sulfonate groups was investigated. In this study, the modification of the apical iodide ligands of the crystalline Mo_6 cluster precursor ($Cs_2[Mo_6I_8]$) was carried out by using $(-OSO_2-C_{10}H_6-SO_3^-)$ (NS) anions with two sulfonate groups. In general, the apical I ligand could be replaced by water molecules in a dispersing medium of acetone and distilled water to form a slightly modified cluster $[Mo_6I_8I_4(H_2O)_2]$ [19, 33]. The addition of functional $(-OSO_2-C_{10}H_6-SO_3^-)$ groups to the medium should lead to a parallel substitution of the apical iodides to form the $[Mo_6I_8I_6(H_2O)_y(OSO_2-C_{10}H_6-SO_3^-)_{6-y}]^{y-2}$ ($0 \leq y \leq 6$) anionic cluster, which is neutralized by sodium cations. To confirm this exchangeability, the chemical element compositions of the modified Mo_6 cluster were investigated by X-ray spectroscopy (Fig. S1a). Table S2 summarizes the binding energies of the O1s, C1s, S2p, Na1s, Mo3d, and I3d regions that were calibrated using the carbon binding energy at 285 eV. The element compositions of the non-isolated and isolated MINS24 compounds are shown in Table S3. The complete elimination of the Cs^+ counter cation was confirmed after isolation. Moreover, the atomic ratio of the Mo and I atoms of the Mo_6 cluster in the isolated MINS24 compounds was obtained at 6 and 11 while the theoretical value of the Mo_6 precursor is 6 and 14. The elimination of three apical iodide ligands from the cluster precursor was suggested. The energy binding peaks specific to C1s, S2p, and Mo3d were respectively recorded at 285 eV, 168.3 eV, 228.9 ($Mo3d^{5/2}$), and 232.1 eV ($Mo3d^{3/2}$) (Figs. S1b-d). In greater detail, two peaks of Mo3d are specialized for the Mo^{4+} state of the Mo-I bonding of the Mo_6 cluster. According to the deconvolution spectrum of the O1s region in Fig.

1
2
3
4
5
6 1a and calculated data listed in Table S4, three contributions are observed. The binding energy peaks
7 at 533.7 eV and 532.5 eV are assigned, respectively, to O=S and O-H coming from naphthalene
8 sulfonate and H₂O apical ligands of the Mo₆ cluster. The peak centered at 530.9 eV is attributed to the
9 formation of the O-Mo bonds due to the substitution of the O-containing apical ligands [34]. As seen
10 in Fig. 1b, the deconvoluted energy peaks denoted for inner and apical iodide ligands (Iⁱ and I^a) are
11 indicated at 620.5 eV (3d^{5/2}) and 632.0 eV (3d^{3/2}) and 618.9 eV (3d^{5/2}) and 630.4 eV (3d^{3/2}),
12 respectively. From Table S5, the calculated amount of the inner and apical iodides is 8 and 3 atoms,
13 respectively, which agrees with 11 apical iodides in Table S3. Based on the deconvolution of the XPS
14 spectra of O1s and I3d regions, a new cluster with the formula [Mo₆I₈I₃(H₂O)_y(OSO₂-C₁₀H₆-SO₃⁻)_a-
15 y]^{y-2} (0 ≤ y ≤ 3), which is neutralized by sodium cations, is proposed. As seen in the element of
16 compositions of MINS24 from Table S3, the sodium cations after isolation are realized at 3 atoms per
17 one Mo₆ cluster unit. It is suggested that the MINS24 compound should include a cluster with the
18 formula [Mo₆I₈I₃(H₂O)₂(OSO₂-C₁₀H₆-SO₃⁻ Na⁺)^a] and Na₂(OSO₂-C₁₀H₆-SO₃⁻) molecule at similar
19 percentages.
20
21
22
23
24
25
26
27
28
29

30 **Fig. 1c** provides information about the Raman spectra of the MI and isolated MINS compounds with
31 specific assignments for the Mo-I and Mo-Mo bonds in the wavenumber range from 50 to 400 cm⁻¹.
32 According to the calculated data for the [{Mo₆I₈}I₆] cluster reported by Schoonover et al., the
33 proposed assignments are presented in Table S6. Considering the Raman shifts of MI, specific
34 assignments recorded at 109 and 285 cm⁻¹ belong to the symmetry vibration of the Mo-Mo bond of
35 the octahedral Mo₆ cluster. The Raman shifts of Mo-I^a and Mo-Iⁱ are recorded at 126 (Mo-Iⁱ, Mo-I^a),
36 154.8 (Mo-Iⁱ, A_{1g}), and 223 (Mo-Iⁱ). In addition, the vibrational signals assigned to the Mo-O bonding
37 appear at 487, 564, 726, and 955 cm⁻¹ (**Fig. 1d**) [35]. Based on the NS reference sample, the Raman
38 shift bands centered at 521 (C-C-C bending), 1054, and 1381 cm⁻¹ (C-C stretching) are assigned to the
39 C-C bond in naphthalene; 611 and 1119 cm⁻¹ assigned to the S-O bond in the sulfonate (-SO₃⁻) group;
40 1468 (C-H bending), 1566, and 1624 cm⁻¹ assigned to the C-C and C=C stretching in an aromatic ring
41 with resonances of the S-O vibrations [36-38]. In general, all the Raman bands of the MINS series
42 show a similar signal. In comparison with the Raman bands of MI and NS, the MINS band is composed
43 of vibration signals of its compositions with a slight modification. The recognition of specialized
44 vibrational bands in the spectrum of MINS24 confirms the shift in the Raman peaks at a lower
45 wavenumber for the Mo-Iⁱ, Mo-I^a, Mo-O, S=O, and S-O stretching vibrations. For example, all the
46 Raman peaks assigned to Mo-Iⁱ and Mo-I^a, namely, at 125 (Mo-Iⁱ, Mo-I^a), 151 (Mo-Iⁱ, A_{1g}), and 219
47
48
49
50
51
52
53
54
55
56
57
58
59
60

1
2
3
4
5
6 $\text{cm}^{-1}(\text{Mo-I}^i)$ are shifted towards lower wavenumber values. The contribution of the new Mo-O link
7 thus affects the polarization and atomic distance of the Mo-Iⁱ or Mo-I^a or Mo-Mo links. In addition,
8 the intensity of the Raman peaks centered at 1561 and 1624 cm^{-1} is reversed in MINS24 compared to
9 that of NS (**Fig. 1d**). Both Raman shifts are assigned to the symmetry C=C vibration in the ring that
10 links carbon with the SO_3 stretching. Thus, the shift in the Raman peak from 1566 to 1561 cm^{-1} and
11 the decrease of the signal intensity at 1623 cm^{-1} come from the increase of the defects in the S-O
12 stretching due to the appearance of the possible Mo-O-S link [39]. The reduction of the polar vibrations
13 of the S-O bond results in increasing the Raman scatterers. Fourier-transform infrared spectroscopy
14 (FTIR) curves were obtained between 1300 cm^{-1} and 1000 cm^{-1} that characterize the vibrational band
15 of the SO_3^- group during the interaction with anions (**Fig. 1e**). Most of the symmetric and asymmetric
16 stretching vibrations assigned to SO of the SO_3^- group shift to a lower wavenumber. It is evident that
17 a strong peak at 1046 cm^{-1} comes from the SO shifts to 1042 cm^{-1} and 1030 cm^{-1} after incorporating
18 the Mo_6 cluster. Following the report of Kabiri and co-authors, the SO vibration appeared at around
19 1036 cm^{-1} and indicated the SO vibration in the free SO_3^- group [40]. The addition of sodium or
20 calcium cations will provide ionic interactions that hindered the efficient delocalization of the negative
21 charge on the sulfonate, resulting in the shift to 1044 and 1056 cm^{-1} , respectively. These proofs are
22 meaningful to favor the appearance of the 1042 cm^{-1} and 1030 cm^{-1} peaks coming from SO after
23 separating sodium cations in this study. The intensity of the 1030 cm^{-1} peak is strongly recognized in
24 the case of MINS16 then it reduces for MINS24 and MINS35. The free SO_3^- groups in MINS16 are
25 efficiently generated while the use of high NS amounts in MINS35 does not contribute to the
26 separation of the sodium cations. In summary, as illustrated in Fig. 1f, at least one covalent bond
27 possibly appears between the Mo_6 cluster and NS *via* the Mo-O-S bridge. Moreover, other SO_3^- groups
28 could be paired with sodium cations or create ionic interactions between them that will depend on the
29 added amounts of NS. The balance between the two kinds of ionic interactions possibly controls the
30 aggregation of the nanoparticles that affect the homogeneous dispersion on the semiconductor
31 substrate.
32
33
34
35
36
37
38
39
40
41
42
43
44
45
46
47
48
49
50
51
52
53
54
55
56
57
58
59
60

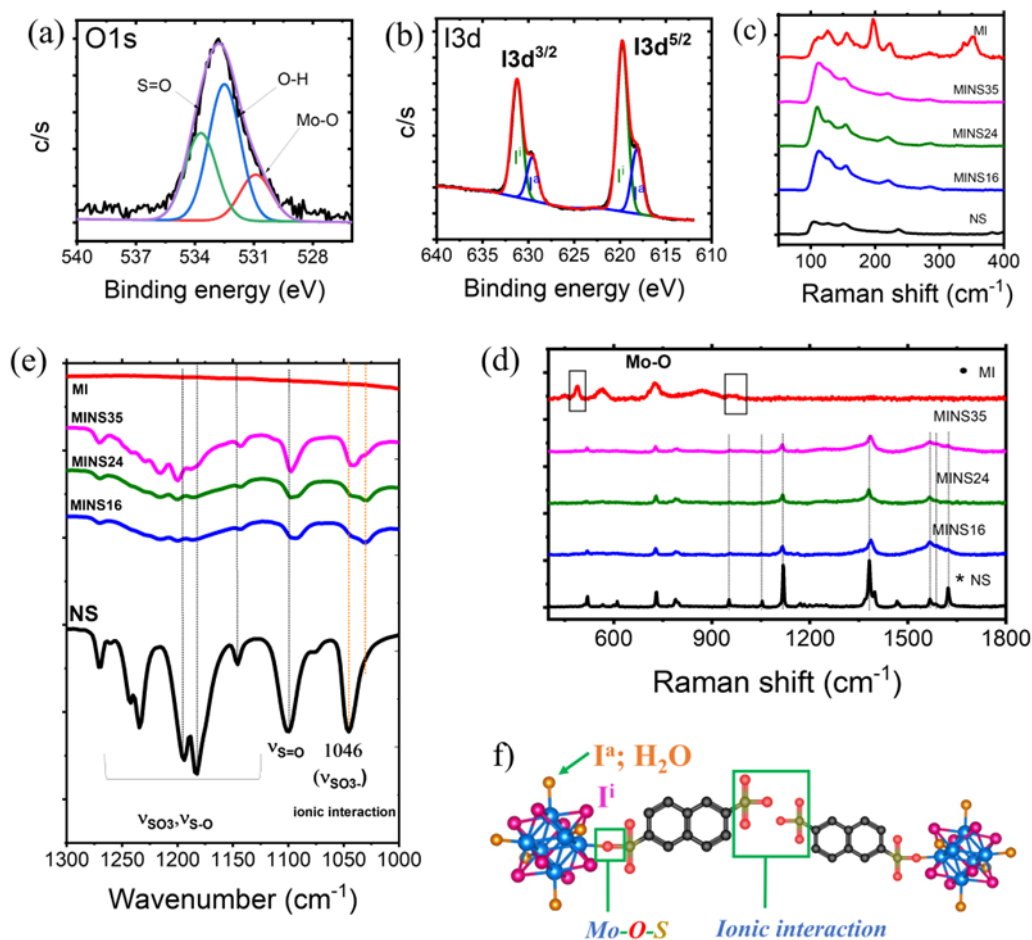


Figure 1. The deconvolution XPS spectra of a) O1s and b) I3d regions of the isolated MINS24. The fingerprint Raman shifts of MI, NS, and isolated MINS_x (x=16, 24, 35) between c) 50 to 400 cm⁻¹ and (d) 500 to 1800 cm⁻¹ in air at 298K. e) Fourier-transform infrared spectroscopy (FTIR) curves between 1300 cm⁻¹ and 1000 cm⁻¹. f) The schematic illustration of the chemical structure of the modified Mo₆ clusters and possible interactions.

The UV-Vis absorption spectra of the isolated MINS_x (x=16, 24, 35) and electrophoretically deposited MI films on ITO-coated glass are summarized in **Fig. 2a**. As known, free NS molecules in the compound do not show absorption in the visible light range so they do not contribute to these absorption characteristics in Fig. 2a. The strong absorbance in the visible light range between 400 nm and 600 nm is realized for the electrophoretically deposited MI mainly containing [Mo₆I₈I₄(H₂O)_a]₂ clusters. The modification of the chemical compositions by replacing the iodide apical ligands results in a significant difference in the optical properties. In greater detail, the reduction of the visible light absorption is recognized for MINS_x (x=16, 24, 35) films in the range between 500 nm and 600 nm.

1
2
3
4
5
6 Consequently, the optical gap energies also result in a clear change for all the MINS_x (x = 16, 24, 35)
7 cluster compounds as seen in **Fig. 2b**. As seen in Table 1, the optical energy gap increases from 2.08
8 eV for MI to around 2.44 eV for MINS16 and 2.6 eV for MINS24 and 35. The energy band gap of the
9 [Mo₆I₈I^a₄(H₂O)^a₂]·mH₂O cluster recorded at 2.08 eV agrees with a previous study for the
10 electrophoretically deposited Mo₆ thin film [19, 27]. In the case of MINS16, two energy gaps were
11 calculated at 2.08 and 2.44 eV, which emphasize an incomplete apical exchange to form the
12 constituting clusters; i.e., [Mo₆I₈I^a₄(H₂O)^a₂] and [Mo₆I₈I^a₃(H₂O)^a₂(-OSO₂-C₁₀H₆-SO₃⁻ Na⁺)^a]. The
13 complete modification from the [Mo₆I₈I^a₄(H₂O)^a₂] cluster to the [Mo₆I₈I^a₃(H₂O)^a₂(-OSO₂-C₁₀H₆-SO₃⁻
14 Na⁺)^a] cluster results in a proper change in the optical bandgap E_g that occurs for the MINS 24 and 35
15 compounds recorded at 2.6 eV.

16
17 To estimate the HOMO and LUMO energies of the new compounds and the electrochemical energy
18 band gap, cyclic voltammetry measurements of the MI and isolated MINS_x (x=16, 24, 35) compounds
19 in acetonitrile with the calibration of the ferrocene/ferrocenium redox system are summarized in Fig.
20 S2 and Table 1. The calculation is illustrated in Section 2.5. The onset of oxidation increases from 1.43
21 for the [Mo₆I₈I^a₄(H₂O)^a₂] cluster to 1.76, 1.78, and 1.73 eV for the MINS16, MINS24 and MINS35
22 suspensions containing the [Mo₆I₈I^a₃(H₂O)^a₂(-OSO₂-C₁₀H₆-SO₃⁻ Na⁺)^a] clusters, respectively. It is
23 evident that the aromatic sulfonate groups increase the stability of the cluster complex toward
24 oxidation in the electrolyte medium. The obtained stability is an advantage for the application of the
25 Mo₆ cluster in solar cells. In the negative potential region, the onset of reduction is similar to around
26 -0.87 eV. The HOMO energies are significantly different between the two kinds of cluster complexes.
27 These results show a similar trend to the reported data for the molybdenum cluster complexes
28 (nBu₄N)₂{[Mo₆X₈}X₆ (X⁻ = Cl⁻, Br⁻, I⁻) that have exchanged apical ligands by different aromatic
29 sulfonate ligands [20]. The E_{HOMO} and E_{LUMO} of the modified Mo₆ complexes were systematically
30 tuned by changing the electron-donating naphthalene and electron-withdrawing sulfonate in NS [41].
31 In greater detail, the electron-withdrawing sulfonate group will contribute to the reduction of E_{HOMO}
32 from -5.8 eV to -6.1 eV [42, 43]. It causes a decrease in the electron-electron repulsion that modifies
33 the strength of the Mo-Mo bonds and electronegativity of the Mo₆ octahedron. The electrochemical
34 energy bandgaps calculated from cyclic voltammetry (CV) graphs in Table 1 are relatively similar to
35 the optical energy bandgap that was calculated from the Tauc plot (**Fig. 2b**). In summary, the CV-
36 derived HOMO and LUMO energy levels of the Mo₆-based sensitizers are presented in Fig. 2c. These
37 LUMO energies of the MI and isolated MINS_x (x= 16, 24, 35) compounds are much higher than the
38
39
40
41
42
43
44
45
46
47
48
49
50
51
52
53
54
55
56
57
58
59
60

conduction band (CB) of the semiconductor (-4.0 eV for anatase phase TiO₂), while the HOMO energies are lower than the oxidation potential of the I⁻/I₃⁻ electrolyte (-4.8 eV). This results in the possibility of electron injection into the semiconductor in the photovoltaic device [44]. In line with previous studies, the modified sulfonate-based Mo₆ cluster could be a good candidate for a photostable photosensitizer that provides the excited electrons to generate a short-circuit current in the MCSSCs.

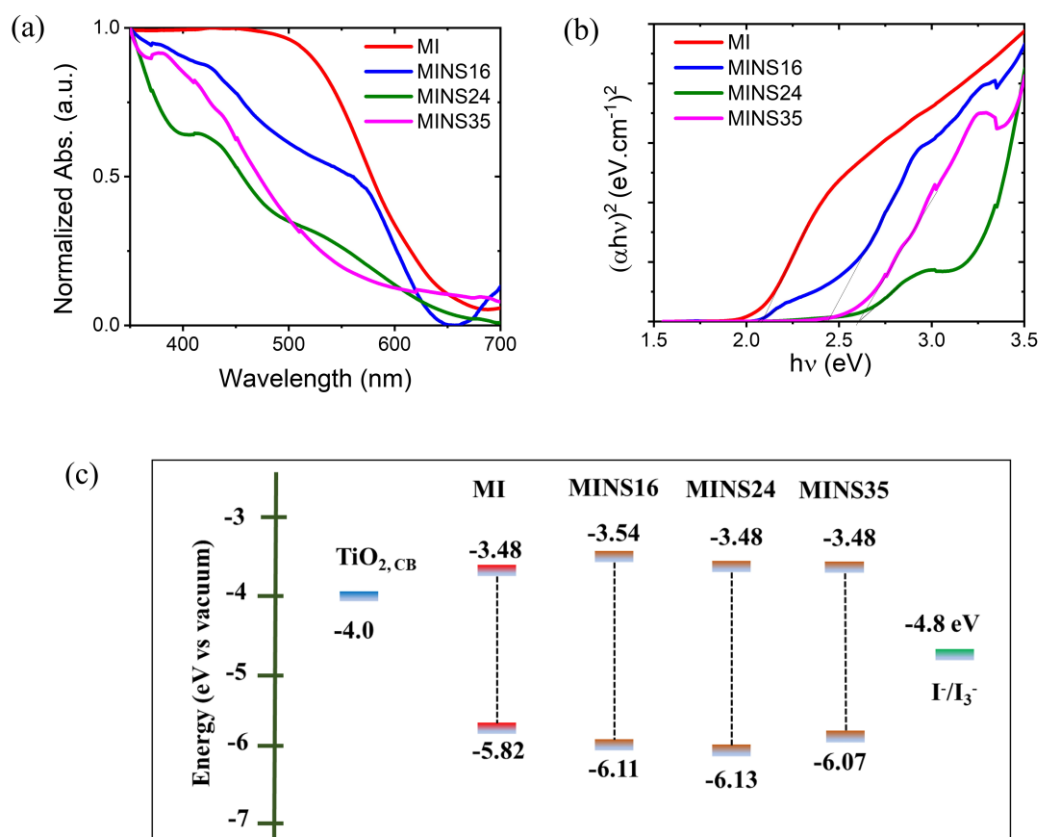


Figure 2. a) The absorption spectra of MI and isolated MINS_x (x = 16, 24, 35) on ITO-coated glass and b) the Tauc plots calculated from the absorption spectra for estimating the optical energy gap. c) CV-derived HOMO and LUMO energy levels vs vacuum of the Mo₆-based sensitizers.

Table 1. The potential of the onset of oxidation ($E_{\text{onset, ox}}$) and reduction ($E_{\text{onset, red}}$) and electrochemical energy band gap of the compound MI after EPD and isolated MINS_x (x = 16, 24, 35). The optical energy gap was calculated from the Tauc plot.

Composites	$E_{\text{onset, ox}}$ vs Ag/AgCl	HOMO level	$E_{\text{onset, red}}$ vs Ag/AgCl	LUMO level	Electrochemical energy	Optical energy gap (eV)
					-cal energy	gap (eV)

	(V)	(V)	(V)	gap (eV)		
MI	1.47	-5.82	-0.87	-3.48	2.34	2.08
MINS16	1.76	-6.11	-0.81	-3.54	2.57	2.08; 2.44
MINS24	1.78	-6.13	-0.87	-3.48	2.65	2.59
MINS36	1.72	-6.07	-0.87	-3.48	2.59	2.60

Photophysical properties of the Mo₆ cluster-based photoelectrodes.

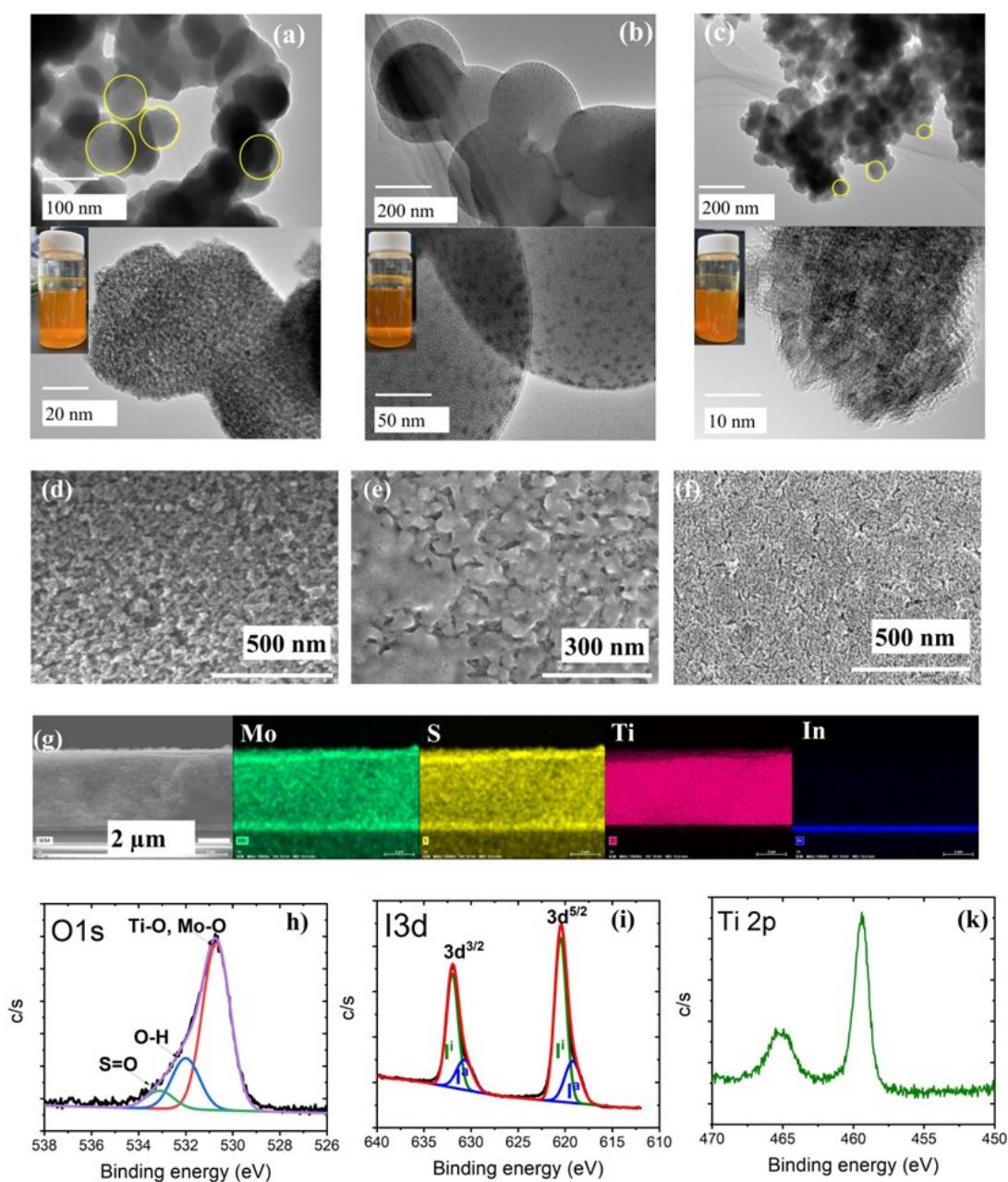
The isolated MINS_x (x = 16, 24, 35) compounds were strongly aggregated after purification to eliminate the residual NS molecules and heat treatment at 50°C. The homogeneous dissolution was impossible to obtain in any solvent media. For that reason, the non-isolated MINS_x slurries were directly used to deposit on the TiO₂ photoelectrodes to achieve a good uniform dispersion. As seen in the HR-TEM images of nanoparticles in the non-isolated MINS_x slurries, the role of residual free NS molecules is discussed (Figs. 3a-c). The trends of the aggregated nanoparticles are different at various ratios of the NS and Mo₆ cluster precursors. The NS amount in MINS16 is efficient for reducing big Mo₆ crystals into nanoparticles sized from 70 to 100 nm while images of the MINS24 show a homogeneous dispersion of 5 nm-sized nanoparticles in the amorphous matrix containing the NS molecules. An increase in the NS amount of MINS35 causes an aggregation between these phases that disturbs the uniform dispersion of the modified Mo₆ cluster. It is evident that only the MINS24 slurries show a relative transparency (Fig. 3a-c). In general, in the solvent medium, big 1 μm-sized Cs₂[{Mo₆I₈}I₆] crystals will be dissociated to form Cs⁺ and [{Mo₆I₈}I₆]²⁻ ions. These [{Mo₆I₈}I₆]²⁻ ions tend to change a neutral [Mo₆I₈I₄(H₂O)^a₂] cluster form that has strong hydrogen bonding causing an aggregation. In MINS24, most of the [Mo₆I₈I₄(H₂O)^a₂] cluster is modified to the [Mo₆I₈I₃(H₂O)^a₂(-OSO₂-C₁₀H₆-SO₃⁻Na⁺)^a] cluster surrounded by the negative charged NS that results in only an ionic interaction, preventing the aggregation. The elimination of residual NS surrounding MINS will destroy the monodispersed distribution that hinders the absorbed sensitizer amounts.

In this study, the titanium (IV) chloride surface treatment on TiO₂ was performed to improve the charge transport, thus enhancing the photovoltaic performance [31, 45]. The optical energy bandgap of TiO₂ was measured at 3.43 eV by using the Tauc plots in Figure SI3a which were almost similar to the previous report [46]. The mesoporous TiO₂ film with the essential anatase crystalline phase was

1
2
3
4
5
6 successfully prepared by thermal treatment at 550 °C in air and its morphology was demonstrated in
7 Figs. S3b and 3d. The surface of the transparent TiO₂-based photoelectrodes is observed to have a
8 roughness as well as high porosities that provide efficient active areas for anchoring the Mo₆ cluster.
9 These patterns are stable and the porous morphology between the nanoparticles is connected after
10 being treated with the TiCl₄ solution (Fig. 3e). MI was deposited on the TiO₂ film by EPD for 2
11 minutes at 20 V. Compared to the soaking method, the EPD was reported as the best method to
12 chemisorb the homogeneous MI into the TiO₂ mesoporous electrodes [19]. In the case of the non-
13 isolated MINS_x (x = 16, 24, 35) clusters dissolved in water/acetone, a vacuum impregnation process
14 for 15 minutes was applied for the depositions because it was not successfully deposited by EPD. The
15 distribution of MI into the cross-section area of the mesoporous TiO₂ film was demonstrated by using
16 TEM-EDX mapping (Fig. S4). Besides the amount of MI adsorbed inside the TiO₂ pores, the thick
17 layer of MI could be recognized on the top of the TiO₂ surface with a thickness of 0.7 μm. Similar
18 layer structures were confirmed in the TiO₂-introduced MINS16 clusters by cross-section SEM images
19 (Fig. S5). The MINS16-based photoelectrode possesses a thickness of 5.6 μm of which about 0.5 μm
20 is only composed of MINS16 on the top. Fig. 3f shows the smooth and homogeneous distribution of
21 MINS24 on the surface of the TiO₂ film. These top cluster layers decrease in the MINS24-based film
22 and disappear in the MINS35-based film (Fig. S6). The elemental compositions of the cross-section
23 clarify the concentration of MINS16 as seen in Fig. S15 and MINS24 in Fig. 3g. A highlight-colored
24 layer assigned to the Mo, I, and S atoms properly appears on the top of the MINS16 while it does not
25 focus on the top of the MINS24 film. Considering the similar deposition method for MINS16, 24, and
26 35 with a similar concentration of the [Mo₆I₁₄] precursor, the difference in the deposition comes from
27 the different number of NS molecules. The increase in the concentration of the NS functional groups
28 seems to improve the adsorption of the cluster inside the pores and reduces the aggregation of clusters
29 on the surface.

30
31
32
33
34
35
36
37
38
39
40
41
42
43
44
45
46
47
48 The elemental compositions and binding energy were measured for the MINS24 deposited on the TiO₂
49 film, showing the stability of the apical ligands after being introduced into the TiO₂ electrode (Tab.
50 S3). The deconvolution spectra of the O1s regions and calculated data presented in Figs. 3h and Table
51 S7 indicate the existence of binding energies assigned to the Mo-O and Ti-O links at about 530.7 eV,
52 O-H at 532 eV, and O=S at 533.1 eV. The ratio between Mo and I at 6 and 11 means the link between
53 MINS and the TiO₂ lattice should come from the sulfonate groups (SO₃⁻) on NS (Tab. S8 and Fig. 3i).
54 The binding energy spectrum of the Ti region shows two spin-orbit peaks of 2p^{3/2} (459.4 eV) and 2p^{1/2}
55
56
57
58
59
60

(465.2 eV) (**Fig. 3k**). It is difficult to show the difference in the binding energy of the Ti-O bonding in TiO₂ or Ti-O-cluster links. The possible prediction for the linking between the SO₃ group-functionalized cluster and TiO₂ lattice could occur; the SO₃ group reacted with the OH groups on the lattice and eliminated water produced during heating at 120 °C to form a Ti-O-S(O₂)-cluster bridge. This covalent interaction should favor the charge transport inside the photoelectrode and should lead to a higher efficiency of photovoltaic devices.



1
2
3
4
5
6 Figure 3. HR-TEM images at different magnifications and photographs of non-isolated slurries under
7 visible light irradiation of a) MINS16, b) MINS24, and c) MINS35. Scanning electron microscopy
8 (SEM) images of d) mesoporous TiO₂-based film, e) mesoporous TiO₂-based film treated with TiCl₄
9 0.3M, f) the non-isolated MINS24-coated TiO₂ photoelectrode. g) the SEM-EDX mapping of the
10 cross-section of non-isolated MINS24-coated TiO₂ photoelectrode. The multiplet split components of
11 h) XPS O1s spectrum, i) XPS I3d spectrum, and (k) XPS Ti2p spectrum.
12
13
14
15
16
17
18

19 The evaluation of the photosensitizer efficiency in solar cells relates to the emission maximum
20 wavelength (λ_{em}), photoluminescence lifetime (τ_{em}) as well as the excited state lifetime and quantum
21 yield (Φ_{em}). To identify the photoluminescent property (PL) of the Mo₆ cluster in solar cells, crystalline
22 MI or isolated MINS-coated quartzs were irradiated under 365 nm UV light (Fig. 4a). The PL intensity
23 of MI is weak while well-distinguished peaks centered at 638, 642, and 646 nm appear for the isolated
24 MINS_x (x= 16, 24, 35), respectively. These broadly obtained PL emissions belong to the wavelength
25 range from 580 nm and 700 nm that is excited by light irradiation lower than 500 nm (Fig. 4b). This
26 large Stoke shift will limit the loss of the absorption photonic energy. These results agree with the
27 previous report on the exchange of different aromatic sulfonate ligands [20]. In summary, the
28 enhancement of the PL signal in MINS means an increase in the contribution of the radiative
29 recombination process compared to the non-radiative recombination [47]. Non-radiative
30 recombination is an unwanted process in the photovoltaic characteristics due to lowering the light
31 generation efficiency by phonon scattering and increasing heat losses.
32
33
34
35
36
37
38
39
40
41

42 Time-resolved photoluminescence (TRPL) signals were recorded via Time-Correlated Single Photon
43 Counting (TCSPC) in air at 298 K. The luminescence emissions of the MI and MINS_x (x= 16, 24, 35)
44 composites are indicated at the wavelength of 700 nm and 640 nm irradiated under 361 nm UV light,
45 respectively. The decay time profiles of MI and MINS crystalline on quartz or TiO₂ are presented in
46 Fig. S7-8. The luminescence lifetimes were fitted by 2 exponential decays for MI-based samples and
47 3-exponential decays for the MINS_x-based samples summarized in Table S9 and (Fig. 4c). The fitted
48 data of MI deposited on quartz show an average emission lifetime (τ_e) of 1.172 μ s that includes a high
49 real percentage of about 98.1 % ($\tau_1 = 58$ ns) and the other is 1.9 % ($\tau_2 = 58.7$ μ s). This is in agreement
50 with the emission lifetime of the Mo₆-based clusters reported in the μ s range [20, 26]. The shorter
51 lifetime is caused by the aggregated clusters while another comes from the monodispersed clusters.
52
53
54
55
56
57
58
59
60

1
2
3
4
5
6 The emission lifetimes of the isolated MINS_x (x = 16, 24, 35) deposited on quartz were fitted by a 3-
7 exponential decay calculation. The contribution of the emission lifetime (τ_3) in the μs range is almost
8 zero while a new and short emission lifetime (τ_2) in the ns range appears as seen in Table S9.
9 Apparently, the photoexcited electron density could be rearranged and trapped by the π -spacer group
10 as naphthalene of MINS, thus tuning the photo-driven electron transport and shortening the lifetime
11 (τ_2) [48-49]. Consequently, the average lifetimes were calculated at 27, 47, and 60 ns for the isolated
12 MINS16, MINS24 and MINS35, respectively. This trend is reversed in the non-isolated MINS_x
13 samples deposited on quartz and relatively similar emission lifetimes were calculated at 48, 47, and
14 41 ns. Generally, the NS molecules contribute to the reduction of the emission lifetime by the electron-
15 withdrawing sulfonate groups. The sulfonate acceptors on NS in MINS possibly accelerate the
16 recombination rate of the excited electrons causing a slight decrease in the emission lifetime with
17 different amounts of NS. The sulfonate functional group has already been investigated as an acceptor
18 to balance the charge carrier transport, enhance the moisture resistance, and reduce the migration of
19 photosensitizers for enhancing the performances of perovskite solar cells [50, 51].

20
21 In order to deeply understand how the charge recombination on the Mo₆ cluster occurs on the interface
22 of the photoelectrode, the luminescence lifetimes of the MI and non-isolated MINS clusters
23 homogeneously deposited on the mesoporous TiO₂ photoelectrode were investigated (Fig. 4c). As
24 demonstrated in Tab. 1, the LUMO energies of MI and MINS are -3.48 eV which are compatible with
25 the injection into the conduction band (CB) at -4.0 eV of TiO₂. All the emission lifetimes of MI and
26 non-isolated MINS compounds deposited on the TiO₂ substrate result in a reduction the same as the
27 increase in the recombination rate by 2 times. MI obviously shows an efficient electron injection into
28 the CB of TiO₂ when the emission decreases from 1170 ns to 72 ns. This electron injection rate
29 increases by 3 times after introducing NS molecules (~ 21 ns). MINS35 obtains a saturated
30 recombination rate (~ 20 ns). As discussed before, the compositions of the sensitizer adsorbed in TiO₂
31 will be composed of [Mo₆I₈I^a₃(H₂O)₂(OSO₂-C₁₀H₆-SO₃⁻ Na⁺)^a] and free Na₂(OSO₂-C₁₀H₆-SO₃⁻)
32 molecules for MINS24 and the free NS molecules will increase more in MINS35. Here, NS plays
33 some essential roles for improving the electron injection: i) the free NS improves the adsorption and
34 homogeneous distribution of MINS on the surface of the lattice, and ii) NS incorporated with the MI
35 cluster efficiently orientates the photoexcited electron on the Mo₆ cluster to the conduction band of
36 TiO₂ via the Mo-O-(OSO₂-C₁₀H₆-SO₂)-O-Ti link [52]. The concentration of free NS molecules in
37 MINS24 conducts a fast injection of the photoinduced electron into the TiO₂ photoelectrode that
38
39
40
41
42
43
44
45
46
47
48
49
50
51
52
53
54
55
56
57
58
59
60

continues to accelerate the injection of the higher free NS concentration in MINS35. It is predicted that the electron-withdrawing sulfonate contributes to the recombination of the photoinduced electrons. Interestingly, many studies have reported efforts to prolong the emission lifetime of sensitizers to higher than 0.1 ns while the Mo_6 cluster is feasible to adjust the emission decay time in the range from ns to μs by changing the apical ligand [16].

As expected, an increase of the quantum yield (Φ_{em}) with the functionalization of the cluster with NS and almost similar values at different NS ratios are due to an increase in the radiative recombination or photoluminescence signal (**Fig. 4d**). In general, free NS molecules only show an optical absorption in the UV range with a peak centered at 314 nm in a water solution and thus shows no contribution to the absorbance of MINS in the visible range higher than 400 nm (Fig. S9a). NS also does not affect the optical characteristic of the TiO_2 photoelectrode as seen in Fig. S9b. These low quantum yield values are recorded at about 1.2 % due to the high scattering from solid crystals.

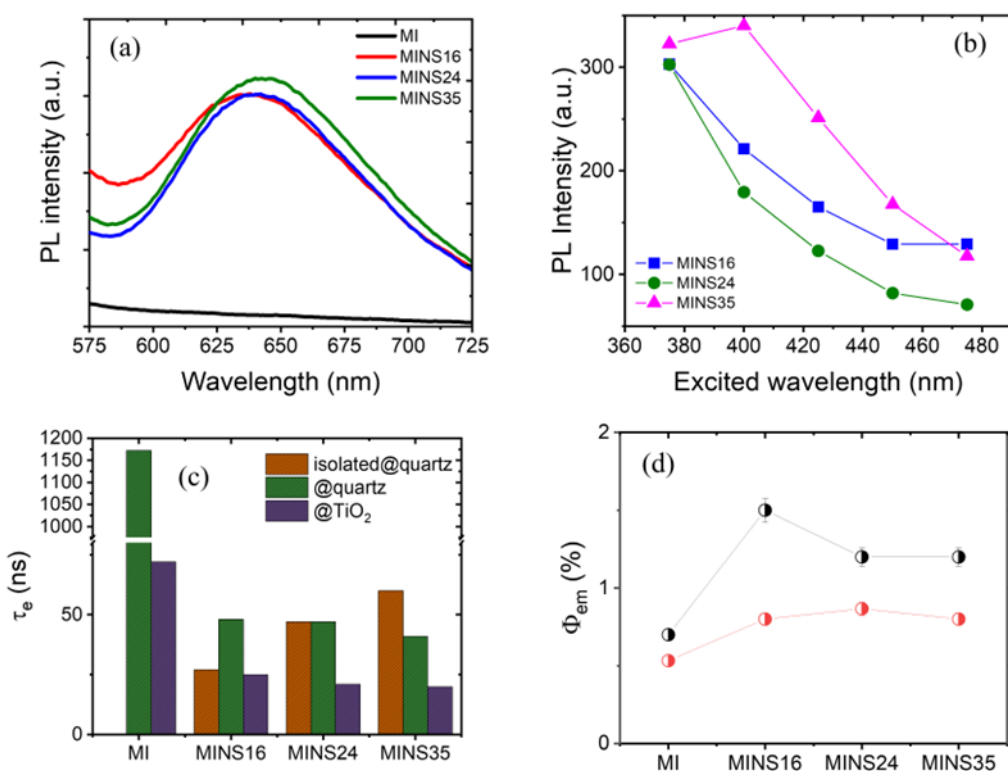


Figure 4. a) Emission spectra of the MI and isolated MINS x ($x=16, 24, 35$) compounds deposited on quartz under irradiation at 365 nm UV light. b) The luminescent emission intensity of the isolated MINS x upon light illumination at different wavelengths. c) Average emission lifetime and d) quantum

1
2
3
4
5
6 yield of MI and non-isolated or isolated MINS_x deposited on quartz (black circles) and TiO₂ substrate
7 (red circles) under excitation at 361 nm.
8
9

10 Photovoltaic characteristics of the Mo₆ cluster-based photoelectrodes.

11
12 The J-V characteristic of MCSSCs was measured for a photoanode containing the TiO₂ layer adsorbed
13 MI and MINS_x (x=16, 24, 35) clusters at about 5- μ m thickness (Fig. 5). A series of isolated MINS_x
14 (x= 16, 24, 35)-based MCSSCs were performed for reference. The short-circuit current (J_{sc}), open-
15 circuit voltage (V_{oc}), fill factor (FF), and power conversion efficiency (η) are listed in Table S110 and
16 **Fig. 5a**. The MI and isolated MINS-based MCSSCs show different J_{sc} and V_{oc} values. In a previous
17 report, an electrophoretically MI-based MCSSC was reported with V_{oc} values of 529 mV, J_{sc} of 1.13
18 mA/cm², FF of 74 and η of 0.44% [19]. In this study, an electrophoretically MI-based MCSSC, with
19 similar I/I₃⁻ electrolyte compositions, was remade under similar conditions. The photovoltaic
20 parameters were measured at 600 mV, 1.76 mV, 50 and 0.52 % for the MI-based MCSSC. As
21 demonstrated in Table S10, all the isolated MINS-based MCSSCs present a reduction in J_{sc} , however,
22 FF definitely increases from 0.5 for MI to 0.65. It is evident of an enhancement of the charge transfer
23 through NS which is linked with the Mo₆ cluster. Only the MINS24-based cell shows a higher overall
24 efficiency (0.58%) compared to the MI-based cell. This result proves the role of NS in enhancing the
25 photoexcited electron injection process from the cluster to CB of the semiconductor. It agrees with a
26 discussion of the emission lifetime parts. Although the slight change of the PV parameters in cells
27 occurred during continuous measurement under irradiation for 330s, the overall efficiency was
28 retained. Fig. S10 presents the morphologies and nanoparticle dispersion of the isolated MINS16 and
29 MINS24. It is a fact that the 1 μ m-sized big nanoparticles and most of the small nanoparticles were
30 deposited on the surface of the TiO₂ substrate. This is a result of a weak dissolution in the solvent
31 medium seen in Fig. S10. The interface connection between the absorbed Mo₆ cluster and the active
32 site of TiO₂ is not efficient.
33
34
35
36
37
38
39
40
41
42
43
44
45
46
47
48

49 Fig. 5b and Table 2 demonstrate the photovoltaic characteristics of the non-isolated MINS_x-based
50 MCCSCs. MI and MINS16 give a slightly different short circuit current J_{sc} of about 1.76 and 1.95
51 mA.cm⁻², respectively, but the fill factor is enhanced from 0.5 to 0.59 for the MINS16-based MCSSC.
52 The improvement of the fill factor with the appearance of the NS ratios tends towards the first
53 hypothesis. Moreover, this phenomenon occurs without an increase in the recombination rate since the
54 V_{oc} is stable. This result provides proof for the discussion in Fig. 4c with the positive effect of the NS
55
56
57
58
59
60

1
2
3
4
5
6 on electron transport and electron injection efficiencies. As a result, the PCE of MINS16-based
7 MCSSC increases by 31% compared to the previous study [25]. the MINS35-based MCSSC shows
8 the highest short circuit current J_{sc} of $2.56 \text{ mA}\cdot\text{cm}^{-2}$ corresponding to the highest PEC of 0.97 % while
9 the fill factor of MINS24-based MCSSC is more efficient. Considering the short-circuit current J_{sc} ,
10 MINS35 obtains a good ratio between MI and NS for a high PEC at 0.97 %, increasing 90 % in
11 comparison to the MI-based MCSSC. The incident photo-to-current efficiency (IPCE) plots of MI and
12 non-isolated MINS $_x$ ($x=16, 24, 35$)-based cells provide proof that supports the high PCE of the
13 MINS24 and MINS35-based cells (Fig. 5c). For a comparison of the PV performance of the non-
14 isolated and isolated MINS $_x$ - based MCSSCs, the NS linked with the Mo_6 cluster will enhance FF the
15 same as the electron injection while the free surrounding NS will enhance the Mo_6 absorption and
16 photocurrent.

17
18 The efficient IPCE in the visible light range is obtained for MINS24 and 35 recorded at 23 % with a
19 wavelength centered at 430 nm and 7% with a wavelength centered at 500 nm. Using an electron-
20 donating organic monolayer at an organic/inorganic interface has proven the induction of the band
21 bending that depends on the adsorbing molecule concentration [53]. The effect of band bending will
22 accelerate the electron transfer at the interface of the NS-modified Mo_6 cluster to the TiO_2
23 semiconductor until equilibrium is reached [54, 55]. In this study, the concentration of the free NS
24 molecules is controlled to obtain the optimal effect of band bending for charge transfer efficiency.

25
26 Interestingly, the MI and non-isolated MINS $_x$ ($x = 16, 24, 35$) -based cells first showed the rising trend
27 of PCE under irradiation of simulated solar light (Fig. 5d). All the cells present a rising tendency of
28 the PCE of about 20 % after various cycles and then retain or gradually reduce. This phenomenon does
29 not occur for the isolated-MINS $_x$ -based MCCSCs. The rising PCE mostly comes from the
30 enhancement of the photocurrent as seen in Tab. 2. The MI-based cell reaches a maximum PCE after
31 80s then gradually decreases until 330 seconds with a PCE (0.44 %) that is lower than that of the first
32 cycle (0.52 %). Here, two points need to be considered; the long emission lifetime (72 ns) of MI can
33 accumulate the photocurrent in the first 80 seconds, then the recombination rate occurs faster than the
34 accumulation rate due to a generation of a new radical composition which catches the excited electron.
35 It is suggested that the water adsorbed in the $[\{\text{Mo}_6\text{I}_8\}\text{I}_4(\text{H}_2\text{O})_2]\cdot x\text{H}_2\text{O}$ cluster of the MI-based cell
36 could be hydrolyzed to form hydroxyl radicals that collect the electrons, suppressing the electrolyte
37 and cluster regeneration. However, this phenomenon does not occur in both the MINS16 and MINS24-
38 based cells that show similar trends of PCE with a peak of the PCE at values of 0.82 % and 1.18% and
39
40
41
42
43
44
45
46
47
48
49
50
51
52
53
54
55
56
57
58
59
60

1
2
3
4
5
6 then retain it up to 330 seconds. The increase in the PCE at the first stage relates to the long emission
7 lifetime of the $\{\text{Mo}_6\text{I}_8\}^{4+}$ core (~ 20 ns), demonstrating a slow recombination of photoexcited
8 electrons on clusters and accumulating in the total current. In the second saturation state, the free
9 naphthalene group on NS around the Mo_6 cluster can trap the electron by electron-electron pulsion
10 and slow down the recombination process on the Mo_6 cluster. At the suitable ratios of the Mo_6 cluster
11 precursor and NS in MINS16 and MINS24, electron-electron pulsion efficiently works and the PCE
12 is retained at 330 seconds of measurement (Fig. 5d). However, the PCE of the MINS35-based cell has
13 a similar trend with MI; reaching a PCE peak at 1.13% then gradually reducing. At higher NS
14 concentrations, the aggregation of NS could occur and the electron-withdrawing sulfonate and
15 electron-donating naphthalene of the free NS can create a competition in charge recombination and
16 charge trapping of the photoinduced electrons. When the electron-withdrawing sulfonate strongly
17 contributes to the charge recombination, regeneration of the cluster will be suppressed resulting in a
18 reduction of the accumulation of the photocurrent as seen in the PCE tendency of the MINS35-based
19 cell. The morphology of the MINS24-based electrode after photovoltaic measurement for 330 seconds
20 and washing the electrolyte by using acetone is presented in Fig. 5e. It can be clarified that the original
21 surface is retained with the confirmation of Mo atoms from the Mo_6 cluster on the surface (Fig. 5f).
22
23 The photovoltaic characteristics can provide interesting information: i) control of the concentration of
24 NS to obtain a suitable emission lifetime for the $\{\text{Mo}_6\text{I}_8\}^{4+}$ core that accumulates the photocurrent, i)
25 NS can enhance the photocurrent J_{sc} and fill factor that comes from the improvement of the electron
26 transport by inducing band bending, and iii) clarify the relation between the MS concentration on the
27 PEC of the MCSSC.
28
29
30
31
32
33
34
35
36
37
38
39
40
41
42
43
44
45
46
47
48
49
50
51
52
53
54
55
56
57
58
59
60

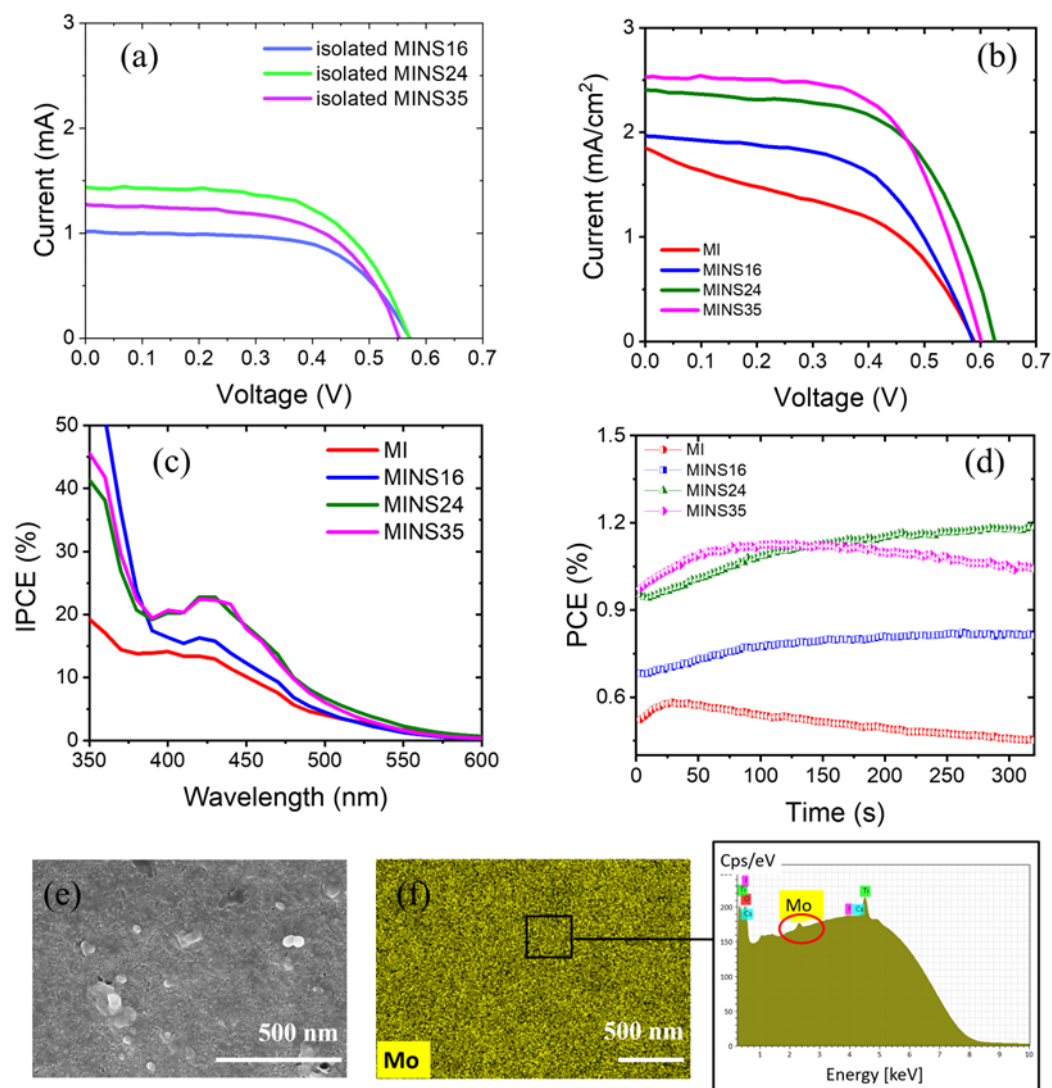


Figure 5. a) J-V characteristic curves of isolated Mo_6 cluster-based-MCCSCs. b) J-V characteristic curves, (c) IPCE curves, and (d) PCE tendency for 100 cycles (330 s) of measurement of non-isolated Mo_6 cluster-based-MCCSCs. E) FE-SEM images and f) SEM-EDX mapping and element spectrum of the non-isolated MINS24-based photoelectrode after irradiation for 330s and elimination of the electrolyte.

Table 2. J-V characteristic of MI and non-isolated MINS_x ($x=16,24,35$) cluster-based MCCSCs at first cycle. Values in brackets were recorded at maximum PCE.

Cell	J_{sc}	V_{oc}	FF	η
	($\text{mA}\cdot\text{cm}^{-2}$)	(mV)		(%)

MI	1.76 (1.96)	600 (600)	0.50 (0.50)	0.52 (0.58)
MINP16	1.95 (2.55)	600 (590)	0.59 (0.54)	0.68 (0.82)
MINP24	2.38 (3.14)	630 (630)	0.63 (0.6)	0.95 (1.18)
MINP35	2.56 (3.22)	610 (600)	0.62 (0.58)	0.97 (1.13)

Electrochemical behaviors of the MI and non-isolated MINS_x (x=16, 24, 35)-based MCSSCs were investigated by measuring the charge transfer resistance R_{ct} , the sheet resistance R_s , and the pseudo capacitance CPE. Fig. 6a shows Nyquist plots of all cells fitted by using the illustrated equivalent circuit. The circuit is composed of two semicircles; the first semicircle corresponds to the substrate resistance (R_{ct1}) for which the onset represents the sheet resistance (R_s) of the photoelectrode and the second semicircle results in the impedance of the cluster/TiO₂/electrolyte interface (R_{ct2}) [31, 56, 57]. Bode plots of the cells provide the maximum angular frequency (ω_{max}) that is used to calculate the electron lifetime in the cells (Fig. 6b). Nyquist and Bode plots were measured in the frequency range from 100 kHz to 0.1 Hz at the open-circuit voltage (V_{oc}) of 600 mV under dark conditions. The charge recombination (τ_{rec}) ability at the cluster/TiO₂/electrolyte interface competes with the charge transport (τ_{trans}). The electron lifetime (τ_{rec}) is associated with ω_{max} in an equation; $\tau_{rec} = 1/(2\pi f)$. The calculated data are summarized in Tab. 3. It was clarified that MI with the longest recombination time (49.8 ms) is beneficial to suppressing the charge recombination on the cluster/TiO₂/electrolyte interface. The increase in the NS concentration causes a reduction in the charge recombination time (< 1 ms), however, it causes a decrease in R_{ct2} corresponding to an improvement in the injection efficiency. The higher chemical capacitance ($C\mu$) of the MI-based cells results in the efficient suppression of the trapping/de-trapping process of the injected electrons in the conduction band of TiO₂ [58]. Although NS negatively affects the suppression of the trapping/de-trapping process, the MINS 24-based MCSSC shows the fastest electron transport (τ_{trans}) of 4.2 μ s that is faster by 15 times in comparison to MI ($\tau_{trans} = 64.6 \mu$ s). This transfer rate starts to be saturated for the MINS35-based cells ($\tau_{trans} = 5.7 \mu$ s). It is consistent with the performances of the MINS24 and 35-based cells. The competition of the electron lifetime in electrolyte and electron transfer by using NS produces a good improvement in the PCE. For that reason, the control of the NS concentration is necessary in the investigations to improve the PCE. In summary, the charge collection efficiency (η_{cc}) derived from $\eta_{cc} = (1 + \tau_{trans} / \tau_{rec})^{-1}$ is about 99 % of all cells which is a beneficial characteristic for obtaining a high efficiency for photovoltaic devices [59, 60].

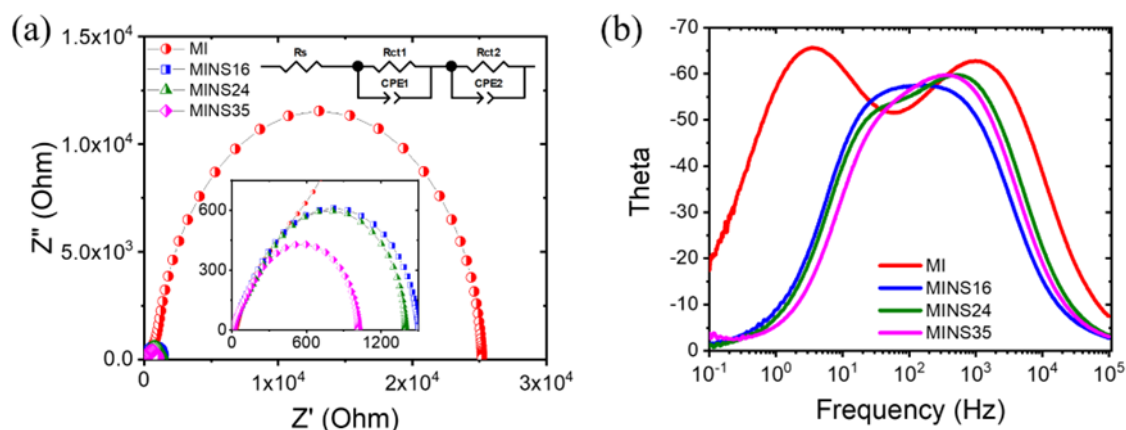


Figure 6. (a) Nyquist plots and equivalent circuits used for fitting the cell impedance and (b) Bode plots of the MI and non-isolated MINS_x-based MCSSCs (x=16, 24, 35).

Table 3. Comparison of EIS parameters of the MI and non-isolated MINS_x-based cells (x=16, 24, 35); sheet resistance R_s , charge transfer resistance R_{ct} , and electrochemical capacitance CPE.

Cells based	R_s (Ω)	R_{ct2} (Ω)	ω_{max} (Hz)	τ_{rec} (ms) $\tau_{rec} = 1/(2\pi f)$	C_μ (μF) $C_\mu = \tau_{rec}/R_{ct2}$	τ_{trans} (μs) $\tau_{trans} = C_\mu R_s$	η_{cc} (%)
MI	31.4	24142	3.2	49.8	2.06	64.6	99.9
MINS16	13.7	1188	144.5	1.1	0.93	12.7	98.9
MINS24	11.6	1157	380.1	0.42	0.36	4.2	99.0
MINS35	11.8	859	380.1	0.42	0.49	5.7	98.6

Although it is a challenge to improve the photovoltaic performance of metal atom cluster-based solar cells, this study has proved the possibility and understood the impact of the physicochemical properties of the cluster for improving the efficiency. In connection with the study, apical ligand groups on the cluster play an important role in enhancing the charge transfer which strongly contributes to the photovoltaic efficiency. For further strategies, some suggestions are proposed to obtain a higher efficiency, for example, the ligands should contain the electron donating groups functionalization; the co-sensitized dye will be investigated with the cluster; the maximal exchange to 6 apical ligands while retaining the visible absorption will be considered; different electrolytes will be used for improving the interaction with the cluster, etc.

4. Conclusion

1
2
3
4
5
6 The Mo₆-based MCSSCs were investigated for their photophysical, photoelectrochemical, and
7 photovoltaic behaviors with the addition of aromatic sulfonate functional groups for the first time. The
8 Mo₆ cluster was functionalized naphthalene-2,6-disulfonate (NS) groups by employing the chemical
9 solution method at different molar ratios of the precursors. The study confirmed that the as-synthesized
10 compounds were composed of the Mo₆-based clusters with the formula of [Mo₆I₈I₃(H₂O)₂(-OSO₂-
11 C₁₀H₆-SO₃⁻ Na⁺)^a] and free Na₂(-OSO₂-C₁₀H₆-SO₃⁻) molecules. The broad absorbance in the visible
12 range was lower than 500 nm, the photoluminescent emission had wavelengths centered around 640
13 nm, and the photoluminescence lifetime in the ns range on the TiO₂ substrate were verified as a
14 function versus the concentration of the introduced NS. NS played a vital role in stabilizing the cluster
15 in the redox mediator, increasing the distribution of the Mo₆-based photosensitizers in TiO₂, and
16 improving the charge transfer process in the redox mediator. As a result, the MINS-based MCSSC
17 resulted in a PCE of 0.97 % which was enhanced by 90 % in comparison to the MI-based cell.
18 Interestingly, this PCE reached the highest value of 1.18 % and then became saturated at the highest
19 value after 330 seconds of measurement for the best cell. A deep understanding of photophysical and
20 photoelectrical behaviors is the original step in targeting the improvement of the efficiency of
21 optoelectronic devices. The first basic knowledge of this study will open a new pathway for research
22 on the improvement of the power conversion efficiency of MCSSCs based on octahedral transition
23 metal clusters.
24
25
26
27
28
29
30
31
32
33
34
35
36
37

38 ASSOCIATED CONTENT

39
40
41 Supporting Information. XPS binding energy and deconvolution spectra; The cyclic voltammetry
42 diagrams; XRD pattern of the TiO₂ film; cross-section SEM and SEM-EDX mapping images of the
43 photoelectrode; Decay time profiles of the transient absorbance.
44
45
46

47 AUTHOR INFORMATION

48 Corresponding Author

49
50
51 Thi Kim Ngan NGUYEN, International Center for Young Scientists, National Institute for Materials
52 Science (NIMS), 1-2-1 Sengen, Tsukuba, Ibaraki 305-0047, Japan
53

54 E-Mail address: NGUYEN.Thikimngan@nims.go.jp
55

56 Author Contributions

57
58
59
60

1
2
3
4
5
6 Thi Kim Ngan Nguyen conceived and designed the experiments; performed the experiments, analyzed
7 and interpreted the data, and drafted the article. Fabien Grasset, Stephane Cordier and Adèle Renaud
8 analyzed and interpreted the data; and drafted the article. Noée Dumait performed the CMI synthesis.
9 Satoshi Ishii, Hiroshi Fudouzi, and Tetsuo Uchikoshi critically revised to improve the intellectual
10 content.
11
12
13
14
15

16 Acknowledgments

17
18 These studies were carried out under the continued financial support of the International Center for
19 Young Scientists (ICYS-Sengen), NIMS, and the France-Japan International Collaboration
20 Framework (IRL3629 LINK, ANR-22-CE09-0015). T.K.N Nguyen would like to thank Dr. Suzuki
21 Tohru for the laboratory supply, Dr. Naoto Shirahata for his useful advice on photoluminescence decay
22 measurements and Dr. Irem Nur Gamze Ozbilgin for the PL decay and Raman's measurements. This
23 study was supported by "Advanced Research Infrastructure for Materials and Nanotechnology in
24 Japan (ARIM)" of the Ministry of Education, Culture, Sports, Science and Technology (MEXT);
25 Proposal Number 23NM5289.
26
27
28
29
30
31
32

33 Notes

34
35
36 The authors declare no competing financial interest.
37
38

39 References

- 40
41 1. Munoz-Garcia; A. B., Benesperi; I., Boschloo; G., Concepcion; J. J., Delcamp; J. H., Gibson; E.A.,
42 Meyer; G.J., Pavone; M., Pettersson; H., Hagfeldt; A., Freitag; M. Dye-sensitized solar cells strike
43 back. *Chem. Soc. Rev.*, 2021, 50, 12450-12550.
44
45 2. Sharma; K., Sharma; V., Sharma; S. S., Dye-Sensitized Solar Cells: Fundamentals and Current
46 Status. *Nanoscale Research Letters*, 2019, 13, 381-427.
47
48 3. Bade; B.R., Kore; K. B., Rondiya; S. R., Nilegave; D. S., Nasane; M.P., Jathar; S. B., Barma; S. V.,
49 Jadkar; S. R., Funde; A. M., Room Temperature Synthesis of Formamidinium Lead Iodide (FAPbI₃)
50 Perovskite for Low-Cost Absorber in Solar Cells. *ES Energy & Environment*, 2021, 13, 31-36.
51
52 4. Ma; Y., Zhang; Y, Liu; M., Han; T., Wang; T., Wang; X., Improving the performance of quantum
53 dot sensitized solar cells by employing Zn doped CuInS₂ quantum dots. *Adv. Composites and Hybrid*
54 *Mater.*, 2022, 5, 402–409 (2022).
55
56 5. O'Regan; B., Grätzel; M. A low-cost, high-efficiency solar cell based on dye-sensitized colloidal
57
58
59
60

1
2
3
4
5
6 titanium dioxide films. *Nature*, 1991, 353, 737–740.

7 6. Sen; A., Putra; M.H., Biswas; A.K., Behera; A. K., Groß; A., Insight on the choice of
8 sensitizers/dyes for dye sensitized solar cells: A review. *Dyes and Pigments*, 2023, 213, 111087.

9
10 7. Lin; L., Li; X., Zhang; H., Xu B.B., Wasnik; P., Li; H., VirSingh; M., Ma; Y., Li; T., Guo; Z.,
11 Research progress of MXenes and layered double hydroxides for supercapacitors *Inorg. Chem. Front.*,
12 2023,10, 4358-4392.

13
14 8. Hou; X., Aitola; K., Lund; P. D. TiO₂ nanotubes for dye-sensitized solar cells—A review. *Energy*
15 *Science & Engineering*, 2020, 9, 921-937.

16
17 9. Ren; Y., Zhang; D., Suo; J., Cao; Y., Eickemeyer; F. T., Vlachopoulos; N., Zakeeruddin; S. M.,
18 Hagfeldt; A., Grätzel; M., Hydroxamic acid pre-adsorption raises the efficiency of cosensitized solar
19 cells. *Nature*, 2023, 613, 60-65.

20
21 10. Song; H., Lin; Y., Zhang; Z., Rao; H., Wang; W., Fang; Y., Pan; Z., Zhong; Z., Improving the
22 Efficiency of Quantum Dot Sensitized Solar Cells beyond 15% via Secondary Deposition. *J. Am.*
23 *Chem. Soc.*, 2021, 12, 4790–4800.

24
25 11. Chen; J. S., Choi; H., Kamat; P.V., Metal-Cluster-Sensitized Solar Cells. A New Class of Thiolated
26 Gold Sensitizers Delivering Efficiency Greater Than 2%. *J. Am. Chem. Soc.*, 2013, 135, 8822–8825.

27
28 12. Abbas; M. A., Kim; T.S., Lee; S.U., Kang; Y. S., Bang; J. H., Exploring Interfacial Events in Gold-
29 Nanocluster-Sensitized Solar Cells: Insights into the Effects of the Cluster Size and Electrolyte on
30 Solar Cell Performance. *J. Am. Chem. Soc.*, 2016, 138, 390–401.

31
32 13. Sakai; N., Ikeda; T., Teranishi; T., Tatsuma; T., Sensitization of TiO₂ with Pt, Pd, and Au Clusters
33 Protected by Mercapto- and Dimercaptosuccinic Acid. *Chem. Phys. Chem.*, 2011, 12, 2415-2418.

34
35 14. Jennings; J. R., Liu; Y., Wang; Q., Efficiency Limitations in Dye-Sensitized Solar Cells Caused by
36 Inefficient Sensitizer Regeneration. 2011, *J. Phys. Chem. C*, 115, 15109–15120.

37
38 15. Zhou; P., Liang; J., Lin; B., An; Z., Chen; R., Chen, X.; An; Q., Chen; P., Effect of the Spatial
39 Configuration of Donors on the Photovoltaic Performance of Double D- π -A Organic Dyes. *ACS Appl.*
40 *Mater. Interfaces*, 2021, 13, 40648–40655.

41
42 16. Zohry; A. E., Orthaber; A., Zietz; B., Isomerization and Aggregation of the Solar Cell Dye D149.
43 *J. Phys. Chem. C*, 2012, 116, 26144–26153.

44
45 17. Warnan; J., Pellegrin; Y., Blarta; E., Odobel; F. Supramolecular light-harvesting antennas to
46 enhance absorption cross-section in dye-sensitized solar cells. *Chemical Communication*, 2012, 48,
47 675-677.

48
49 18. Renaud; A., Grasset; F., Dierre; B., Uchikoshi; T., Ohashi; N., Takei; T., Planchat; A., Cario; L.,
50
51
52
53
54
55
56
57
58
59
60

- 1
2
3
4
5
6 Jobic; J., Odobel; F., Cordier; S., Inorganic Molybdenum Clusters as Light-Harvester in All Inorganic
7 Solar Cells: A Proof of Concept. *Chemistry Select*, 2016, 1, 2284-2289.
- 8
9 19. Renaud; A., Nguyen; T.K.N., Grasset; F., Raissi; M., Guillon; V., Delabrouille, F., Dumait; N.,
10 Jouan; P.Y., Cario; L., Jobic; S., Pellegrin; Y., Odobel; F., Cordier; S., Uchikoshi; T. Preparation by
11 electrophoretic deposition of molybdenum iodide cluster-based functional nanostructured
12 photoelectrodes for solar cells. *Electrochimica Acta*, 2019, 317, 737-745.
- 13
14 20. Efremova; O.A., Vorotnikov; Y.A., Brylev; K.A., Vorotnikova; N.A., Novozhilov; I.N., Kuratieva;
15 N.V., Edeleva; M.V., Benoit; D.M., Kitamura; N., Mironov; Y.V., Shestopalov; M.A., Sutherland; A.J.
16 Octahedral molybdenum cluster complexes with aromatic sulfonate ligands. *Dalton Trans*, 2016, 45,
17 5427–15435.
- 18
19 21. Cordier; S., Grasset; F., Molard; Y., Amela-Cortes; Boukherroub; M. R., Ravaine; S., Mortier; M.,
20 Ohashi; N., Saito; N., Haneda; H., Inorganic Molybdenum Octahedral Nanosized Cluster Units,
21 Versatile Functional Building Block for Nanoarchitectonics. *Inorg. Organomet. Polym. Mater.*, 2015,
22 25, 189–204.
- 23
24 22. Nguyen; T.K.N., Lebastard; C., Wilmet; M., Dumait; N., Renaud; R., Cordier; S., Ohashi; N.,
25 Uchikoshi; T., Grasset; F., A review on functional nanoarchitectonics nanocomposites based on
26 octahedral metal atom clusters (Nb6, Mo6, Ta6, W6, Re6): inorganic 0D and 2D powders and films.
27 *STAM*, 2022, 23, 547–578.
- 28
29 23. Lappi; T., Cordier; S., Gayfulin; Y., Girard; S.A., Grasset; F., Uchikoshi; T., Naumov; N.G.,
30 Renaud; A., Nanoarchitectonics of Metal Atom Cluster-Based Building Blocks Applied to the
31 Engineering of Photoelectrodes for Solar Cells. *Solar RRL*, 2023, 7, 2201037.
- 32
33 24. Nguyen; T. K. N., Dumait; N., Grasset; F., Cordier; S., Berthebaud; D., Matsui; Y., Ohashi; N.,
34 Uchikoshi; T., Zn–Al Layered Double Hydroxide Film Functionalized by a Luminescent Octahedral
35 Molybdenum Cluster: Ultraviolet–Visible Photoconductivity Response. *ACS Applied Materials &*
36 *Interfaces*, 2020, 12, 40495-40509.
- 37
38 25. Guégan; G., Cheng; X., Huang; X., Němečková; Z., Kubáňová; M., Zelenka; J., Ruml; T., Grasset;
39 F., Sugahara; Y., Lang; K., and Kirakci; K., Graphene Oxide Sheets Decorated with Octahedral
40 Molybdenum Cluster Complexes for Enhanced Photoinactivation of *Staphylococcus aureus*. *Inorg.*
41 *Chem.* 2023, 62, 14243–14251.
- 42
43 26. Nguyen; T.K.N., Grasset; F., Cordier; S., Dumait; N., Ishii; S., Fudouzi; H., Uchikoshi; T., Light
44 harvesting hexamolybdenum cluster integrated with the 3D ordered semiconductor inverse opals for
45 optoelectronic property. *Materials Today Chemistry*. 2023, 27, 101351.
- 46
47
48
49
50
51
52
53
54
55
56
57
58
59
60

- 1
2
3
4
5
6 27. Renaud; A., Jouan; P. Y., Dumait; N., Girard; S.A., Barreau; N., Uchikoshi; T., Grasset; F., Jobic;
7 S., Cordier ; S., Evidence of the Ambipolar Behavior of Mo(6) Cluster Iodides in All-Inorganic Solar
8 Cells: A New Example of Nanoarchitectonic Concept. *ACS Appl. Mater. Interfaces*, 2022, 14, 1347–
9 1354.
10
11
12 28. Lladó; E.A., Tabernig; A.S., Veeken; T., Garnett; E. C., Polman; A., Ehrler; B., Photovoltaics
13 Reaching for the Shockley–Queisser Limit. *ACS Energy Lett.* 2020, 5, 3029–3033.
14
15 29. Kirakci; K., Nguyen; T.K.N., Grasset; F., Uchikoshi; T., Zelenka; J., Kubát; P., Ruml; T., Lang; K.,
16 Electrophoretically Deposited Layers of Octahedral Molybdenum Cluster Complexes: A Promising
17 Coating for Mitigation of Pathogenic Bacterial Biofilms under Blue Light. *ACS Appl. Mater.*
18 *Interfaces*, 2020, 12, 52492–52499.
19
20
21 30. Kirakci; K., Cordier; S., Perrin; C., Synthesis and Characterization of Cs₂Mo₆X₁₄ (X = Br or I)
22 Hexamolybdenum Cluster Halides: Efficient Mo₆ Cluster Precursors For Solution Chemistry
23 Syntheses. *Z. Anorg. Allg. Chem.*, 2005, 63, 411-416.
24
25 31. Sharif; N.F.M., Shafie; S., Kadir; M.Z.A. Ab., Hasan; W.Z. W., Mustafa; M.N., Samaila; B., The
26 effect of titanium (IV) chloride surface treatment to enhance charge transport and performance of dye-
27 sensitized solar cell. *Results in Physics*, 2019, 15, 102725.
28
29 32. Pomrnerehne; J., Vestweber; H., Gun; W., Muhrt; R.E., Bassler; H., Porsch; M., Daub; J., Efficient
30 Two Layer LEDs on a Polymer Blend Basis. *Adv. Mater.*, 1995, 7, 551-554.
31
32 33. Vorotnikova; Y.A., Efremovab' O.A., Novozhilova; I.N., Yansholec; V.V., Kuratieva; N.V., Brylev;
33 K.A., Kitamura; N., Mironov; Y.V., Shestopalov; M.I., Hexaazide octahedral molybdenum cluster
34 complexes: Synthesis, properties and the evidence of hydrolysis. *Journal of Molecular Structure*, 2017,
35 1134, 237-243.
36
37 34. White; R.T.; Thibau; E.S., Lu; Z.H., Interface Structure of MoO₃ on Organic Semiconductors. *Sci.*
38 *Rep.*, 2016, 6, 21109.
39
40 35. Kumari; L., Ma; Y.R., Tsai; C.C., Lin; Y.W., Wu; S.Y., Cheng; K.W., Liou; Y., X-ray diffraction
41 and Raman scattering studies on large-area array and nanobranched structure of 1D MoO₂ nanorods.
42 *Nanotechnology*; 2007, 18, 115717.
43
44 36. Mabrouk; K.B., Kauffmann; T.H., Aroui;H., Fontana; M.D., Raman study of cation effect on
45 sulfate vibration modes in solid state and aqueous solutions. *J. Raman Spectroscopy*, 2013, 44, 1603-
46 1608.
47
48 37. Choi; J., Ahn; D.S., Fujitsuka; M., Tojo; S., Ihee; H., Majima; T. Formation of the Charge-
49
50
51
52
53
54
55
56
57
58
59
60

- 1
2
3
4
5
6 Localized Dimer Radical Cation of 2-Ethyl-9,10-dimethoxyanthracene in Solution Phase. *Chem. Eur.*
7 *J.*, 2019, 25, 5586 – 5594.
8
9 38. Šetka; M., Calavia; R., Vojkůvka; L., Llobet; E., Drbohlavová; J., Vallejos; S., Raman and XPS
10 studies of ammonia sensitive polypyrrole nanorods and nanoparticles. *Sci. Rep.*, 2019, 9, 8465.
11
12 39. Virgilio; M.D., Peressut; A.B., Latorrata; S., Mariani; M., Dotelli; G., Graphene oxide-naphthalene
13 sulfonate blends as possible proton exchange membranes. *Solid State Ionics*, 2022, 376, 115858.
14
15 40. Kabiri; K., Zohuriaan-Mehr; M. J., Mirzadeh; H., Kheirabadi; M., Solvent-, ion- and pH-specific
16 swelling of poly(2-acrylamido-2-methylpropane sulfonic acid) super absorbing gels, *J. Polym. Res.*,
17 2010, 17, 203–212.
18
19 41. Funaki; T., Otsuka; K., Onozawa-Komatsuzaki; N., Kasuga; K., Sayamaab; K., Sugihara; H.,
20 Systematic evaluation of HOMO energy levels for efficient dye regeneration in dye-sensitized solar
21 cells. *J. Mater. Chem. A*, 2014, 2, 5945-15951.
22
23 42. Zhang; T.T., Jia; J.F., Wu; H.S., Substituent and Solvent Effects on Electronic Structure and
24 Spectral Property of $\text{ReCl}(\text{CO})_3(\text{NAN})$ ($\text{NAN} = \text{Glyoxime}$): DFT and TDDFT Theoretical Studies. *J.*
25 *Phys. Chem. A*, 2010, 114,12251–12257.
26
27 43. Chataigner; I., Panel; C., Gérard; H., Piettre; S.R., Sulfonyl vs. carbonyl group: which is the more
28 electron-withdrawing? *Chem. Commun.*, 2007, 31, 288-3290.
29
30 44. Bledowski; M., Wang;L., Ramakrishnan; A., Khavryuchenko; O.V., Khavryuchenko; V.D., Ricci;
31 P.C., Strunk; J., Cremer; T., Kolbeckf; C., Beranek; R., Visible-light photocurrent response of TiO_2 –
32 polyheptazine hybrids: evidence for interfacial charge-transfer absorption, *Phys. Chem. Chem. Phys.*, ,
33 2011, 13, 21511-21519.
34
35 45. Xu; Y., Gao; C., Tang; S., Zhang; J., Chen; Y., Zhu; Y., Hu; Z., Comprehensive understanding of
36 TiCl_4 treatment on the compact TiO_2 layer in planar perovskite solar cells with efficiencies over 20%.
37 *J. Alloys and Compounds*, 2019, 787, 1082-1088.
38
39 46. Sun; H., Xu; Z.T., Zhang; D., First-principles calculations to investigate doping effects on electrical
40 conductivity and interfacial contact resistance of TiO_2 . *Applied Surface Science*, 2023, 614, 156202.
41
42 47. Cheng; H., Feng; Y., Fu; Z., Zheng; Y., Shao; Y., Bai; Y., Understanding and minimizing non-
43 radiative recombination losses in perovskite light-emitting diodes. *J. Mater. Chem. C*, 2022, 10,
44 13590-13610.
45
46 48. Shalini; S., Balasundaraprabhu; R., Kumar; T. S., Prabavathy; N., Senthilarasu; S., Prasanna; S.
47 Status and outlook of sensitizers/dyes used in dye sensitized solar cells (DSSC): a review. *International*
48 *Journal of Energy Research*, 2016, 40, 1303-1320
49
50
51
52
53
54
55
56
57
58
59
60

- 1
2
3
4
5
6 49. Supur; M., Fukuzumi; S., Tuning the photo-driven electron transport within the columnar
7 perylenediimide stacks by changing the π -extent of the electron donors. *Phys. Chem. Chem. Phys.*,
8 2013, 15, 2539-2546.
9
10 50. Mikhailov; M. A., Brylev; K.A., Abramov; P.A., Sakuda; E., Akagi; S., Ito; A., Kitamura; N.,
11 Sokolov; M. N., Synthetic Tuning of Redox, Spectroscopic, and Photophysical Properties of
12 {Mo6I8}Carboxylate Ligands. *Inorg. Chem.*, 2016, 55, 8437–8445.
13
14 51. Hung; C.M., Lin; J.T., Yang; Y.H., Liu; Y.C., Gu; M.W., Chou; T.C., Wang; S.F., Chen; Z.Q., Wu;
15 C.C., Chen; L.C., Hsu; C.C., Chen; C.H., Chiu; C.W., Chen; H.C., Chou; P.T., Modulation of
16 Perovskite Grain Boundaries by Electron Donor–Acceptor Zwitterions R,R-Diphenylamino-phenyl-
17 pyridinium-(CH₂)_n-sulfonates: All-Round Improvement on the Solar Cell Performance., *J. ACS Au* ,
18 2022, 2, 1189–1199.
19
20 52. Wang; K.L., Lu; H., Li; M., Chen; C.H., Zhang; D.B., Chen; J., Wu; J.J., Zhou; Y.H., Wang; X.Q.,
21 Su; Z. H., Shi; Y.R., Tian; Q.S., Ni; Y.Z., Gao; X. Y., Zakeeruddin; S.M., Grätzel; M., Wang; Z.K.,
22 Liao; L.S., Ion–Dipole Interaction Enabling Highly Efficient CsPbI₃ Perovskite Indoor Photovoltaics.,
23 *Adv. Mater.*, 2023, 35, 2210106.
24
25 53. Rinke, Hofmann; O.T., Patrick, Band Bending Engineering at Organic/Inorganic Interfaces Using
26 Organic Self-Assembled Monolayers. *Adv. Electron.Mater.*, 2017, 3, 1600373.
27
28 54. Schukraft; G.E.M, Moss; B., Kafizas; A.G., Petit; C., Effect of Band Bending in Photoactive MOF-
29 Based Heterojunctions. *ACS Appl. Mater. Interfaces*, 2022, 14, 19342–19352.
30
31 55. Listorti; A., O'Regan; B., Durrant; J. R., Electron Transfer Dynamics in Dye-Sensitized Solar Cells,
32 *Chem. Mater.*, 2011, 23, 3381–3399.
33
34 56. Wang; Q., Moser; J.E., Grätzel' M., Electrochemical Impedance Spectroscopic Analysis of Dye-
35 Sensitized Solar Cells. *J. Phys. Chem. B*, 2005, 109, 14945–14953.
36
37 57. Kim; S.G., Ju; M.J., Choi; I.T., Choi; W.S., Choi; H. J., Baek; J.B., Kim; H.K., Nb-doped TiO₂
38 nanoparticles for organicdye-sensitized solar cells. *RSC Adv.*, 2013, 3, 16380–16386.
39
40 58. Zaine; S.N.A., Mohamed; N.M., Khatani; M., Samsudin; A.E., Shahid; M.U., Trap State and
41 Charge Recombination in Nanocrystalline Passivized Conductive and Photoelectrode Interface of
42 Dye-Sensitized Solar Cell. *Coatings*, 2020, 10, 284.
43
44 59. Nissfolk; S., Fredin; K., Hagfeldt; A., Boschloo; G., Recombination and Transport Processes in
45 Dye-Sensitized Solar Cells Investigated under Working Conditions. *J. Phys. Chem. B*, 2006, 110,
46 17715–17718.
47
48
49
50
51
52
53
54
55
56
57
58
59
60

1
2
3
4
5
6 60. Van de Lagemaat; T.J., Park; N.G., Frank; A. J. Influence of Electrical Potential Distribution,
7 Charge Transport, and Recombination on the Photopotential and Photocurrent Conversion Efficiency
8 of Dye-Sensitized Nanocrystalline TiO₂ Solar Cells: A Study by Electrical Impedance and Optical
9 Modulation, *J. Phys. Chem. B*, 2000, 104, 2044–2052.
10
11
12
13
14
15
16
17
18
19
20
21
22
23
24
25
26
27
28
29
30
31
32
33
34
35
36
37
38
39
40
41
42
43
44
45
46
47
48
49
50
51
52
53
54
55
56
57
58
59
60